



1 **Algorithm Theoretical Baseline for formaldehyde retrievals** 2 **from S5P TROPOMI and from the QA4ECV project.**

3 Isabelle De Smedt¹, Nicolas Theys¹, Huan Yu¹, Thomas Danckaert¹, Christophe Lerot¹,
4 Steven Compernelle¹, Michel Van Roozendael¹, Andreas Richter², Andreas Hilboll², Enno
5 Peters², Mattia Pedergnana³, Diego Loyola³, Steffen Beirle⁴, Thomas Wagner⁴, Henk Eskes⁵,
6 Jos van Geffen⁵, Klaas Folkert Boersma^{5,6}, Peepijn Veeffkind⁵.

7 [1]{Royal Belgian Institute for Space Aeronomy (BIRA-IASB), Brussels, Belgium}

8 [2]{Institute of Environmental Physics, University of Bremen (IUP-B), Otto-Hahn-Allee 1, 28359 Bremen, Germany}

9 [3]{Institut für Methodik der Fernerkundung (IMF), Deutsches Zentrum für Luft und Raumfahrt (DLR), Oberpfaffenhofen, Germany}

10 [4]{ Max Planck Institute for Chemistry (MPIC), Hahn-Meitner-Weg 1, 55128 Mainz, Germany}

11 [5]{KNMI, De Bilt, The Netherlands}

12 [6]{Wageningen University, Meteorology and Air Quality group, Wageningen, The Netherlands}

13 *Correspondence to:* I. De Smedt (isabelle.desmedt@aeronomie.be)

14 **Abstract:** On board of the Copernicus Sentinel-5 Precursor (S5P) platform, the TROPospheric Monitoring
15 Instrument (TROPOMI) is a double channel nadir-viewing grating spectrometer measuring solar back-
16 scattered earthshine radiances in the ultraviolet, visible, near-infrared and shortwave infrared with global daily
17 coverage. In the ultraviolet range, its spectral resolution and radiometric performance are equivalent to those
18 of its predecessor OMI, but its horizontal resolution at true nadir is improved by an order of magnitude. This
19 paper introduces the formaldehyde (HCHO) tropospheric vertical column retrieval algorithm implemented in
20 the S5P operational processor, and comprehensively describes its various retrieval steps. Furthermore,
21 algorithmic improvements developed in the framework of the EU FP7-project QA4ECV are described for
22 future updates of the processor. Detailed error estimates are discussed in the light of Copernicus user
23 requirements and needs for validation are highlighted. Finally, verification results based on the application of
24 the algorithm to OMI measurements are presented, demonstrating the performances expected for TROPOMI.

25 **1. Introduction**

26 Long term satellite observations of tropospheric formaldehyde (HCHO) are essential to support air quality and
27 chemistry-climate related studies from the regional to the global scale. Formaldehyde is an intermediate gas in
28 almost all oxidation chains of non-methane volatile organic compounds (NMVOC), leading eventually to CO₂.
29 NMVOCs are, together with NO_x, CO and CH₄, among the most important precursors of tropospheric ozone.
30 NMVOCs also produce secondary organic aerosols and influence the concentrations of OH, the main
31 tropospheric oxidant. The major HCHO source in the remote atmosphere is CH₄ oxidation. Over the continents,
32 the oxidation of higher NMVOCs emitted from vegetation, fires, traffic and industrial sources results in
33 important and localised enhancements of the HCHO levels (as illustrated in Figure 1). Its lifetime being of the
34 order of a few hours, HCHO in the boundary layer can be related to the release of short-lived hydrocarbons,
35 which mostly cannot be observed directly from space. Furthermore, HCHO observations provide information
36 on the chemical oxidation processes in the atmosphere, including CO chemical production from CH₄ and
37 NMVOCs. The seasonal and inter-annual variations of the formaldehyde distribution are principally related to



38 temperature changes (controlling vegetation emissions) and fire events, but also to changes in anthropogenic
39 activities. For all these reasons, HCHO satellite observations are used in combination with tropospheric
40 chemistry transport models to constrain NMVOC emission inventories in so-called top-down inversion
41 approaches (e.g. Abbot et al., 2003, Palmer et al., 2006; Fu et al., 2007; Millet et al., 2008; Stavrakou et al.,
42 2009a, 2009b, 2012, 2015; Curci et al., 2010; Barkley et al., 2011, 2013; Fortems-Cheiney et al., 2012; Marais
43 et al., 2012; Mahajan et al., 2015).

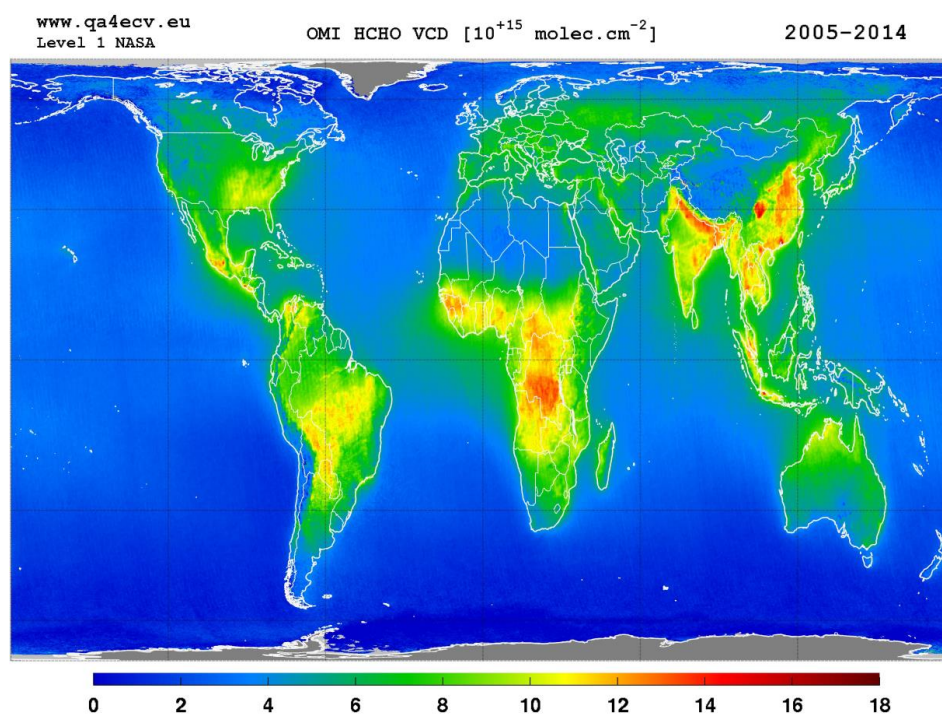
44 HCHO tropospheric columns have been successively retrieved from GOME on ERS-2 and from SCIAMACHY
45 on ENVISAT, resulting in a continuous data set covering a period of almost 16 years from 1996 until 2012
46 (Chance et al., 2000; Palmer et al., 2001; Wittrock et al., 2006; Marbach et al., 2009; De Smedt et al., 2008;
47 2010). Started in 2007, the measurements made by the three GOME-2 instruments (EUMETSAT METOP-A,
48 B and C) have the potential to extend by more than a decade the successful time-series of global formaldehyde
49 morning observations (Vrekoussis et al., 2010; De Smedt et al., 2012; Hewson et al., 2012; Hassinen et al.,
50 2016). Since its launch in 2004, OMI on the NASA AURA platform has been providing complementary HCHO
51 measurements in the early afternoon with daily global coverage and a better spatial resolution than current
52 morning sensors (Kurosu et al., 2008; Millet et al., 2008; González Abad et al., 2015; De Smedt et al., 2015).
53 TROPOMI aims to continue this time series of early afternoon observations, with daily global coverage, a
54 spectral resolution and signal-to-noise ratio (SNR) equivalent to OMI, but combined with a spatial resolution
55 improved by an order of magnitude, which potentially offers an unprecedented view of the spatiotemporal
56 variability of NMVOC emissions.

57 To fully exploit the potential of satellite data, applications relying on tropospheric HCHO observations require
58 high quality long-term time series, provided with well characterized errors and averaging kernels, and
59 consistently retrieved from the different sensors. Furthermore, as the HCHO observations are aimed to be used
60 synergistically with other species observations (e.g. with NO₂ for air quality applications), it is essential to
61 homogenize as much as possible the retrieval methods as well as the external databases, in order to minimize
62 systematic biases between the observations. The design of the TROPOMI HCHO prototype algorithm,
63 developed at BIRA-IASB, has been driven by the experience developed with formaldehyde retrievals from the
64 series of precursor missions OMI, GOME(-2) and SCIAMACHY. Furthermore, within the S5P Level 2
65 Working Group project (L2WG), a strong component of verification has been developed involving independent
66 retrieval algorithms for each operational prototype algorithm. For HCHO, the University of Bremen (IUP-UB)
67 has been responsible of the algorithm verification. An extensive comparison of the processing chains of the
68 prototype (the retrieval algorithm presented in this paper) and verification algorithm has been conducted. In
69 parallel, within the EU FP7-project Quality Assurance for Essential Climate Variables (QA4ECV, Lorente et
70 al., 2017), a detailed step by step study has been performed for HCHO and NO₂ DOAS retrievals, including
71 more scientific algorithms (BIRA-IASB, IUP-UB, MPIC, KNMI and WUR), leading to state-of-the art
72 European products (www.qa4ecv.eu). Those iterative processes led to improvements that have been included
73 in the S5P prototype algorithm, or are proposed as options for future improvements of the operational
74 algorithm.



75 This paper gives a thorough description of the TROPOMI HCHO algorithm baseline, as implemented at the
76 German Aerospace Center (DLR) in the S5P operational processor UPAS-2 (Universal Processor for UV/VIS
77 Atmospheric Spectrometers). It reflects the S5P HCHO Level 2 Algorithm Theoretical Basis Document v1.0
78 and also describes the options to be activated after the S5P launch, as implemented for the QA4ECV OMI
79 HCHO retrieval algorithm (see illustration in Figure 1).

80 In Section 2, we discuss the product requirements and the expected product performance in terms of precision
81 and trueness, and provide a complete description of the retrieval algorithm. In Section 3, the uncertainty of the
82 retrieved columns and the error budget is presented. Results from the algorithm verification exercise are given
83 in Section 4. The possibilities and needs for future validation of the retrieved HCHO data product can be found
84 in Section 5. Conclusions are given in Section 6.



86 **Figure 1: 10-years average of HCHO vertical columns retrieved from OMI between 2005 and 2014**
87 (<http://www.qa4ecv.eu/ecv/hcho-p/data>).



88 2. TROPOMI HCHO algorithm

89 2.1 Product Requirements

90 In the UV, the sensitivity to HCHO concentrations in the boundary layer is intrinsically limited from space due
 91 to the combined effect of Rayleigh and Mie scattering that limit the fraction of radiation scattered back from
 92 low altitudes and reflected from the surface to the satellite. In addition, ozone absorption reduces the number
 93 of photons that reach the lowest atmospheric layers. Furthermore, the absorption signatures of HCHO are
 94 weaker than those of other UV-Vis absorbers, such as e.g. NO₂. As a result, the retrieval of formaldehyde from
 95 space is noise sensitive and error prone. While the precision (or random uncertainty) is mainly driven by the
 96 signal to noise ratio of the recorded spectra, the trueness (or systematic uncertainty) is limited by the current
 97 knowledge on the external parameters needed in the different retrieval steps.

98 The requirements for HCHO retrievals have been identified as part of the TROPOMI science objectives
 99 document (van Weele et al., 2008), the COPERNICUS Sentinels-4/-5 Mission Requirements Document MRD
 100 (Langen et al., 2011; 2017), and the S5P Mission Advisory Group report of the review of user requirements
 101 for Sentinels-4/-5 (Bovensmann et al., 2011). The requirements for HCHO are summarised in Table 1.
 102 Uncertainty requirements include retrieval errors as well as measurement (instrument-related) errors. Absolute
 103 requirements (in total column units) relate to background conditions, while percentage values relate to elevated
 104 columns.

105 Three main COPERNICUS environmental themes have been defined as ozone layer (A), air quality (B), and
 106 climate (C) with further division into sub themes. Requirements for HCHO have been specified for a number
 107 of these sub themes (B1: Air Quality Protocol Monitoring, B2: Air Quality Near-Real Time, B3: Air Quality
 108 Assessment, and C3: Climate Assessment). With respect to air quality protocol monitoring, which is mostly
 109 concerned with trend and variability analysis, the requirements are specified for NMVOC emissions on
 110 monthly to annual time scales and for larger region/country scale (Bovensmann et al., 2011). In the error
 111 analysis section, we discuss these requirements and the expected performances of the HCHO retrieval
 112 algorithm.

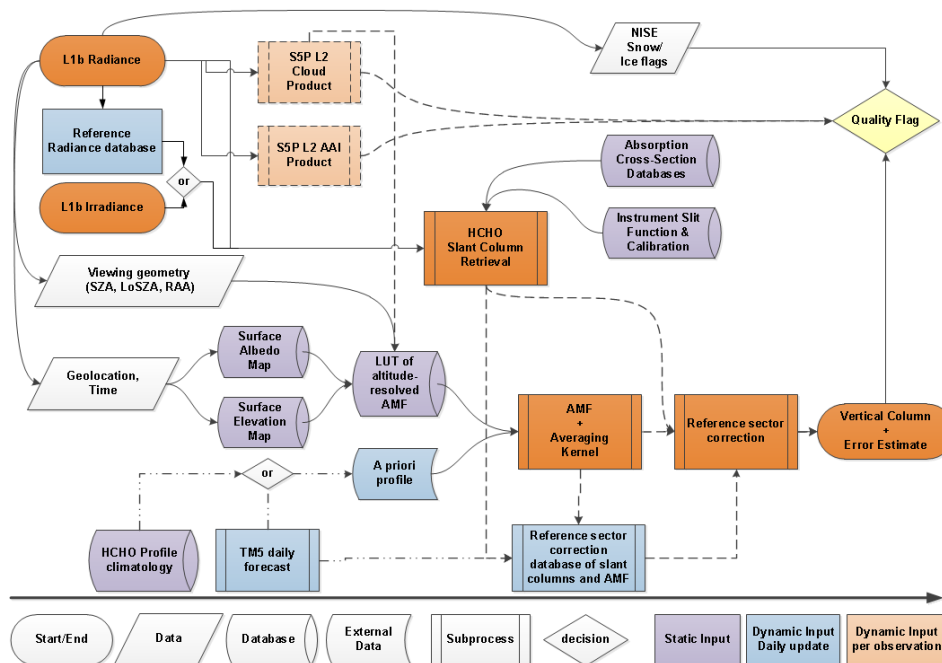
113 **Table 1: Requirements on HCHO vertical tropospheric column products as derived from the MRD.**
 114 **Where numbers are given as "a - b", the first is the target requirement and the second is the threshold**
 115 **requirement.**

Horizontal resolution [km]	Revisit time	Theme	Required uncertainty
5-20	0.5-2h	B1, B2, B3	30-60% or 1.3×10^{15} molec.cm ⁻² (least stringent)
5-50	6 - 24x3 hour	C3	30% or 1.3×10^{15} molec.cm ⁻² (least stringent)

116



117 **2.2 Algorithm description**



118

119 **Figure 2: Flow Diagram of the L2 HCHO retrieval algorithm implemented in the S5P operational**
 120 **processor.**

121 Figure 2 displays a flow diagram of the level-2 (L2) HCHO retrieval algorithm implemented in the S5P
 122 operational processor. The baseline operation flow scheme is based on the Differential Optical Absorption
 123 Spectroscopy (DOAS) retrieval method (Platt et al., 1994; Platt and Stutz, 2008; and references therein). It is
 124 identical in concept to the one of SO₂ (Theys et al., 2017) and very close to the one of NO₂ (van Geffen et al.,
 125 2017). The interdependencies with auxiliary data and other L2 retrievals, such as clouds, aerosols or surface
 126 reflectance are also represented.

127 Following the diagram in Figure 2, the processing of S5P level-1b (L1b) data proceeds as follows: radiance
 128 and irradiance spectra are read from the L1b file, along with geolocation data such as pixel coordinates and
 129 observation geometry (sun and viewing angles). The relevant absorption cross section data as well as
 130 characteristics of the instrument are used as input for the determination of the HCHO slant columns (N_s). In
 131 parallel to the slant column fit, S5P cloud information and absorbing aerosol index (AAI) data are obtained
 132 from the operational chain. Alongside, in order to convert the slant column to a vertical column (N_v), an air
 133 mass factor (M) that accounts for the average light path through the atmosphere is calculated. For this purpose,
 134 several auxiliary data are read from external (operational and static) sources: cloud cover data, topographic
 135 information, surface albedo, and the a priori shape of the vertical HCHO profile in the atmosphere. The AMF
 136 is computed by combining an a priori formaldehyde vertical profile and altitude-resolved air mass factors
 137 extracted from a pre-computed look-up-table (also used as a basis for the error calculation and retrieval
 138 characterization module). This look up table has been created using the VLIDORT 2.6 radiative transfer model



139 (Spurr et al., 2008a) at a single wavelength representative for the retrieval interval. It is used to compute the
140 total column averaging kernels (Eskes and Boersma, 2003), which provide essential information on the
141 measurement vertical sensitivity and are required for comparison with other types of data.

142 Background normalization of the slant columns is required in the case of weak absorbers such as formaldehyde.
143 Before converting the slant columns into vertical columns, background values of N_s are normalized to
144 compensate for possible systematic offsets (reference sector correction, see below). The tropospheric vertical
145 column end product results therefore from a differential column to which is added the HCHO background due
146 to methane oxidation, estimated using a tropospheric chemistry transport model.

147 The final tropospheric HCHO vertical column is obtained using the following equation:

$$N_v = \frac{N_s - N_{s,0}}{M} + N_{v,0} \quad (1)$$

148 The main outputs of the algorithm are the slant column density (N_s), the tropospheric vertical column (N_v), the
149 tropospheric air mass factor (M), and the values used for the reference sector correction ($N_{s,0}$ and $N_{v,0}$).
150 Complementary product information includes the clear sky air mass factor, the error on the total column, the
151 averaging kernel, and quality flags. Table 13 in the appendix B gives a non-exhaustive set of data fields that
152 are provided in the level 2 data product. A complete description of the level 2 data format is given in the S5P
153 HCHO Product User Manual (Pedernana et al., 2017).

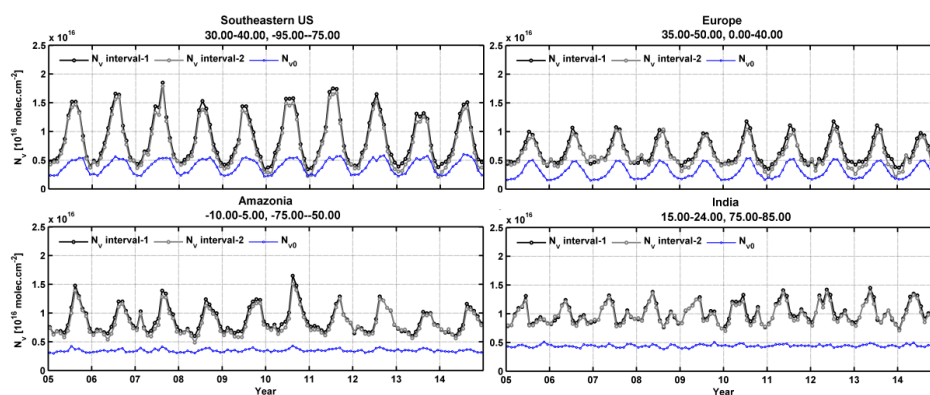
154 Algorithmic steps are described in more details in the next sections, and settings are summarized in Table 2,
155 along with algorithmic improvements developed in the framework of the EU FP7-project QA4ECV and
156 proposed for future TROPOMI processor updates. Figure 3 also presents examples of monthly averaged
157 HCHO vertical columns over four NMVOC emission regions, along with the background correction values.

158 **Table 2 : Summary of algorithm settings used to retrieve HCHO tropospheric columns from**
159 **TROPOMI spectra. The last column lists additional features implemented in the QA4ECV HCHO**
160 **product, which are options for future updates of the S5P Processor.**

Parameter	S5P Operational Algorithm	QA4ECV Algorithm
Slant Columns		
Fitting interval-1	328.5-359 nm	
Fitting interval-2	328.5-346 nm (N_s, BrO fixed by fit in interval-1)	
Absorption cross-sections	HCHO, Meller and Moortgat (2000), 298K NO ₂ , Vandaele et al. (1998), 220K Ozone, Serdyuchenko et al. (2013), 223 + 243K BrO, Fleischmann et al. (2004), 223K O ₂ -O ₂ , Thalman et al. (2013), 293K	
Ring effect	Ring cross-section based on the technique outlined by Chance et al. (1997), defined as I_{rrs}/I_{elas} , where I_{rrs} and I_{elas} are the intensities for inelastic (Rotational Raman Scattering; RRS) and elastic scattering processes.	
Non-linear O3 absorption effect	2 pseudo-cross sections from the Taylor expansion of the ozone slant column into wavelength and the O ₃ vertical optical depth (Puķīte et al., 2010).	



Slit function	One slit function per binned spectrum as a function of wavelength (Pre Flight Model, TROPOMI ISRF Calibration Key Data v1.0.0)	Fit of a prescribed function shape to determine the ISRF during wavelength calibration + online convolution of cross-sections.
Polynomial	5 th order	
Intensity offset correction	Linear offset ($1/I_0$)	
Iterative spike removal	Not activated.	Activated. Tolerance factor 5 (see section 2.2.1)
Reference spectrum I_0	Daily solar irradiance	Daily average of radiances, per row, selected in a remote region.
Air Mass Factors		
Altitude dependent AMFs	VLIDORT , 340 nm, 6-D AMF look-up table	
Treatment of partly cloudy scenes	IPA, no correction for $f_{eff} < 10\%$	
Aerosols	No explicit correction	
A priori profile shapes	TM5-MP $1^\circ \times 1^\circ$, daily forecast (NRT) or reprocessed (Offline)	
Correction of surface pressure	Yes (Equation (10))	
Surface Albedo	OMI-based monthly minimum LER (update of Kleipool et al., 2008)	
Digital elevation map	GMTED2010 (Danielson et al., 2011)	
Cloud product	S5P operational cloud product, treating clouds as Lambertian reflectors (OCRA/ROCINN-CRB, Loyola et al., 2017)	OMI operational cloud algorithm, treating clouds as Lambertian reflectors (O ₂ -O ₂ , Veeffkind et al., 2016)
Background Correction		
Correction equation	$N_{v,0} = N_{v,0,CTM}$	$N_{v,0} = \frac{M_0}{M} N_{v,0,CTM}$ (see section 2.2.3)



161

162 **Figure 3: Example of regional and monthly averages of the HCHO vertical columns over different**
 163 **NMVO emission regions, for the period 2005-2014. Results of the retrievals in the two fitting**
 164 **intervals (-1 and -2) are shown, as well as the magnitude of the background vertical column ($N_{v,0}$).**

165 2.2.1 Formaldehyde slant column retrieval

166 The DOAS method relies on the application of Beer-Lambert's law. The backscattered earthshine spectrum as
 167 measured by the satellite spectrometer contains the strong solar Fraunhofer lines and additional fainter features
 168 due to interactions taking place in the Earth atmosphere during the incoming and outgoing paths of the
 169 radiation. The basic idea of the DOAS method is to separate broad and narrowband spectral structures of the
 170 absorption spectra in order to isolate the narrow trace gas absorption features. In practice, the application of
 171 the DOAS approach to scattered light observations relies on the following key approximations:

- 172 1. For weak absorbers the exponential function can be linearized and the Lambert-Beer law can be
 173 applied to the measured radiance to which a large variety of atmospheric light paths contributes.
- 174 2. The absorption cross-sections are assumed to be weakly dependent on temperature and
 175 independent of pressure. This allows expressing light attenuation in terms of Beer-Lambert's law,
 176 and (together with approximation 1) separating spectroscopic retrievals from radiative transfer
 177 calculations by introducing the concept of one effective slant column density for the considered
 178 wavelength window.
- 179 3. Broadband variations are approximated by a common low-order polynomial to compensate for
 180 the effects of loss and gain from scattering and reflections by clouds/air molecules and/or at the
 181 Earth surface.

182 The DOAS equation is obtained by considering the logarithm of the radiance $I(\lambda)$ and the irradiance $E_0(\lambda)$ (or
 183 another reference radiance selected in a remote sector) and including all broadband variations in a polynomial
 184 function:

$$\ln \frac{I(\lambda)}{E_0(\lambda)} \cong - \sum_j \sigma_j(\lambda) N_{s,j} + \sum_p c_p \lambda^p \quad (2)$$



$$\tau_s^{meas}(\lambda) \cong \tau_s^{diff}(\lambda, N_{s,j}) + \tau_s^{smooth}(\lambda, c_p), \quad (3)$$

185 where the measured optical depth τ_s^{meas} is modelled using a highly structured part τ_s^{diff} and a broadband
 186 variation τ_s^{smooth} .

187 Equation (2) is a linear equation between the logarithm of the measured quantities (I and E_0), the slant column
 188 densities of all relevant absorbers ($N_{s,j}$) and the polynomial coefficients (c_p), at multiple wavelengths. DOAS
 189 retrievals consist in solving an over-determined set of linear equations, which can be done by standard methods
 190 of linear least squares fit (Platt and Stutz, 2008). The fitting process consists in minimizing the chi-square
 191 function, i.e. the weighted sum of squares derived from Equation (3):

$$X^2 = \sum_{i=1}^k \frac{(\tau_s^{meas}(\lambda_i) - \tau_s^{diff}(\lambda_i, N_{s,j}) - \tau_s^{smooth}(\lambda_i, c_p))^2}{\varepsilon_i^2} \quad (4)$$

192 where the summation is made over the individual spectral pixels included in the selected wavelength range (k
 193 is the number of spectral pixels in the fitting interval). ε_i is the statistical uncertainty on the measurement at
 194 wavelength λ_i . Weighting the residuals by the instrumental errors ε_i is optional. When no measurement
 195 uncertainties are used (or no error estimates are available), all uncertainties in Equation (4) are set to $\varepsilon_i = 1$,
 196 giving all measurement points equal weight in the fit.

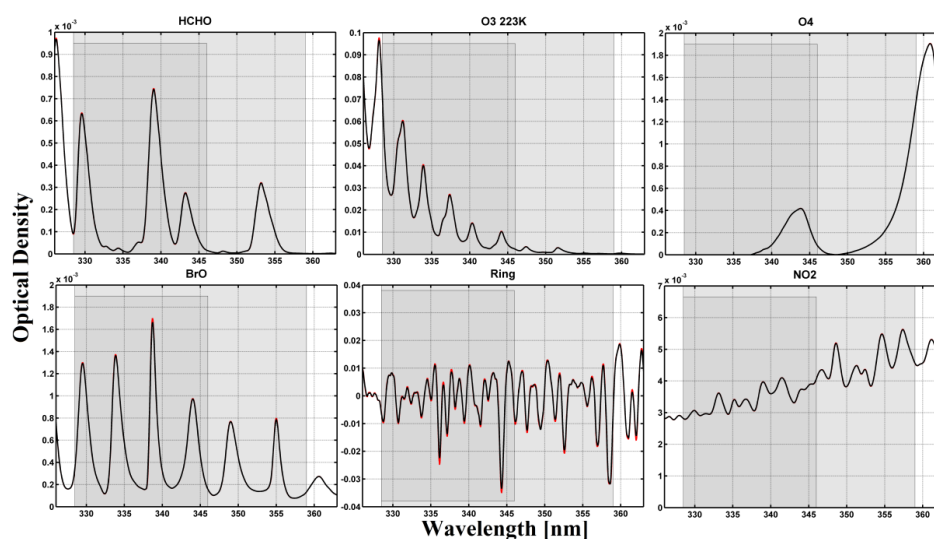
197 In order to optimize the fitting procedure, additional structured spectral effects have to be considered carefully
 198 such as the Ring effect (Grainger and Ring, 1962). Furthermore, the linearity of Equation (3) may be broken
 199 down by instrumental aspects such as small wavelength shifts between I and E_0 .

200 **Fitting intervals, absorption cross-sections and spectral fitting settings**

201 Despite the relatively large abundance of formaldehyde in the atmosphere (of the order of 10^{16} molec.cm⁻²)
 202 and its well-defined absorption bands, the fitting of HCHO slant columns in earthshine radiances is a challenge
 203 because of the low optical density of HCHO compared to other UV-Vis absorbers. The typical HCHO optical
 204 density is one order of magnitude smaller than that of NO₂ and three orders of magnitude smaller than that for
 205 O₃ (see Figure 4). Therefore, the detection of HCHO is limited by the signal to noise ratio of the measured
 206 radiance spectra and by possible spectral interferences and misfits due to other molecules absorbing in the same
 207 fitting interval, mainly ozone, BrO and O₄. In general, the correlation between cross-sections decreases if the
 208 wavelength interval is extended, but the assumption of a single effective light path defined for the entire
 209 wavelength interval may not be fully satisfied, leading to systematic misfit effects that may also introduce
 210 biases in the retrieved slant columns. To optimize DOAS retrieval settings, a trade-off has to be found
 211 minimising these effects taking also into consideration the instrumental characteristics. A basic limitation of
 212 the classical DOAS technique is the assumption that the atmosphere is optically thin in the wavelength region
 213 of interest. At shorter wavelengths, the usable spectral range of DOAS is limited by rapidly increasing Rayleigh
 214 scattering and O₃ absorption. The DOAS assumptions start to fail for ozone slant columns larger than 1500 DU
 215 (Van Roozendaal et al., 2012). Historically, different wavelength intervals have been selected between 325 and



216 360 nm for the retrieval of HCHO using previous satellite UV spectrometers (e.g: GOME, Chance et al., 2000;
 217 SCIAMACHY, Wittrock et al., 2006, or GOME-2, Vrekoussis et al., 2010). The TEMIS dataset combines
 218 HCHO observations from GOME, SCIAMACHY, GOME-2 and OMI measurements retrieved in the same
 219 interval (De Smedt et al., 2008; 2012; 2015). The NASA operational and PCA OMI algorithm exploit a larger
 220 interval (Kurosu, 2008; González Abad et al., 2015, Li et al., 2015). The latest QA4ECV product uses the
 221 largest interval, thanks to the good quality of the OMI level 1 spectra. A summary of the different wavelength
 222 intervals is provided in Table 3.



223

224 **Figure 4: Typical optical densities of HCHO, O₃, O₂-O₂, BrO, Ring effect, and NO₂ in the near UV. The**
 225 **slant columns have been taken as 1.3×10^{16} molec.cm⁻² for HCHO, 10^{19} molec.cm⁻² for O₃, 0.4×10^{43}**
 226 **molec².cm⁻⁵ for O₂-O₂, 10^{14} molec.cm⁻² for BrO, and 1×10^{16} molec.cm⁻² for NO₂. High resolution**
 227 **absorption cross-sections of Table 2 have been convolved with the TROPOMI ISFRs v1.0 (row 1 is shown**
 228 **in red and row 225 in black, see also Figure 5). The two fitting intervals (-1 and -2) used to retrieve**
 229 **HCHO slant columns are limited by grey areas.**

230 **Table 3: Wavelength intervals used in previous formaldehyde retrieval studies [nm].**

	GOME	SCIAMACHY	GOME-2	OMI
Chance et al., 2000	337.5-359			
Wittrock et al., 2006		334-348		
Vrekoussis et al., 2010			337-353	
Hewson et al., 2012			328.5-346	
González Abad et al., 2015; Li et al., 2015				328.5-356.5
De Smedt et al., 2008 ; 2012 ; 2015	328.5-346	328.5-346	328.5-346 (BrO in 328.5-359)	328.5-346 (BrO in 328.5-359)
QA4ECV				328.5-359



231 As for the TEMIS OMI HCHO product (De Smedt et al., 2015), the TROPOMI L2 HCHO retrieval algorithm
232 includes a two-step DOAS retrieval approach, based on two wavelength intervals:

- 233 1. 328.5-359 nm: This interval includes six BrO absorption bands and minimizes the correlation with
234 HCHO, allowing a significant reduction of the retrieved slant column noise. Note that this interval
235 includes part of a strong O₄ absorption band around 360 nm, which may introduce geophysical
236 artefacts of HCHO columns over arid soils or high altitude regions.
- 237 2. 328.5-346 nm: in a second step, HCHO columns are retrieved in a shorter interval, but using the BrO
238 slant column values determined in the first step. This approach allows to efficiently de-correlate BrO
239 from HCHO absorption while, at the same time, the O₄-related bias is avoided.

240 The use of a large fitting interval generally allows for a reduction of the noise on the retrieved slant columns.
241 However, a substantial gain can only be obtained if the level 1 spectra are of sufficiently homogeneous quality
242 over the full spectral range. Indeed, experience with past sensors not equipped with polarization scramblers
243 (e.g. GOME(-2) or SCIAMACHY) has shown that this gain can be partly or totally overruled due to the impact
244 of interfering spectral polarization structures (De Smedt et al., 2012; 2015). Assuming spectra free of spectral
245 features, the QA4ECV baseline option using one single large interval (fitting interval-1) will be applicable to
246 TROPOMI. Results of the retrievals from the two intervals applied to OMI are presented in Figure 3. In this
247 case, vertical column differences between the two intervals are generally lower than 10%. They can however
248 reach 20% in winter time.

249 In both intervals, the absorption cross-sections of O₃ at 223K and 243K, NO₂, BrO and O₄ are included in the
250 fit. The correction for the Ring effect, defined as I_{rrs}/I_{elas} , where I_{rrs} and I_{elas} are the intensities for inelastic
251 (Rotational Raman Scattering; RRS) and elastic scattering processes, is based on the technique published by
252 Chance et al. (1997). Furthermore, in order to better cope with the strong ozone absorption at wavelengths
253 shorter than 336 nm, the method of Puķīte et al. (2010) is implemented. In this method, the variation of the
254 ozone slant column over the fitting window is taken into account. At the first order, the method consists in
255 adding two cross-sections to the fit: $\lambda\sigma_{O_3}$ and $\sigma_{O_3}^2$ (Puķīte et al., 2010; De Smedt et al.; 2012), using the O₃
256 cross-sections at 223K (close to the temperature at ozone maximum in the tropics). It allows a much better
257 treatment of optically thick ozone absorption in the retrieval and therefore to reduce the systematic
258 underestimation of the HCHO slant columns by 50 to 80%, for SZA from 50° to 70°.

259 To obtain the optical density (Equation (2)), the baseline option is to use the daily solar irradiance. A more
260 advanced option, implemented in QA4ECV, is to use daily averaged radiances, selected for each detector row,
261 in the equatorial Pacific (Lat: [-5° 5°], Long: [180° 240°]). The main advantages of this approach are (1) an
262 important reduction of the fit residuals (by up to 40%) mainly due to the cancellation of O₃ absorption and
263 Ring effect present in both spectra; (2) the fitted slant columns are directly corrected for background offsets
264 present in both spectra; (3) possible row-dependent biases (stripes) are directly corrected owing to the use of
265 one reference per detector row; and (4) the sensitivity to instrument degradation is reduced because degradation
266 effects tend to cancel between the analyzed spectra and the references that are used. It must be noted however
267 that the last three effects can be mitigated when a solar irradiance is used as reference, by means of a post-



268 processing treatment applied as part of the background correction of the slant columns (see section 2.2.3). The
269 option of using an equatorial radiance as reference will be activated in the operational processor after the launch
270 of TROPOMI, during the commissioning phase of the instrument.

271 **Wavelength calibration and convolution to TROPOMI resolution**

272 The quality of the DOAS fit critically depends on the accuracy of the wavelength alignment between the
273 earthshine radiance spectrum, the reference (solar irradiance) spectrum and the absorption cross sections. The
274 wavelength registration of the reference spectrum can be fine-tuned to an accuracy of a few hundredths of a
275 nanometer by means of a calibration procedure making use of the solar Fraunhofer lines. To this end, a
276 reference solar atlas E_s accurate in wavelength to better than 0.01 nm (Chance and Kurucz, 2010) is degraded
277 to the resolution of the instrument, through convolution by the TROPOMI instrumental slit function (see Figure
278 5).

279 Using a non-linear least-squares approach, the shift (Δ_i) between the TROPOMI irradiance and the reference
280 solar atlas is determined in a set of equally spaced sub-intervals covering a spectral range large enough to
281 encompass all relevant fitting intervals. The shift is derived according to the following equation:

$$E_0(\lambda) = E_s(\lambda - \Delta_i) \quad (5)$$

282 where E_s is the reference solar spectrum convolved at the resolution of the TROPOMI instrument and Δ_i is the
283 shift in sub-interval i . A polynomial is fitted through the individual points to reconstruct an accurate wavelength
284 calibration $\Delta(\lambda)$ over the complete analysis interval. Note that this approach allows compensating for stretch
285 and shift errors in the original wavelength assignment. In the case of TROPOMI (or OMI), the procedure is
286 complicated by the fact that such calibrations must be performed and stored for each separate spectral field on
287 the CCD detector array. Indeed due to the imperfect characteristics of the imaging optics, each row of the
288 instrument must be considered as a separate detector for analysis purposes.

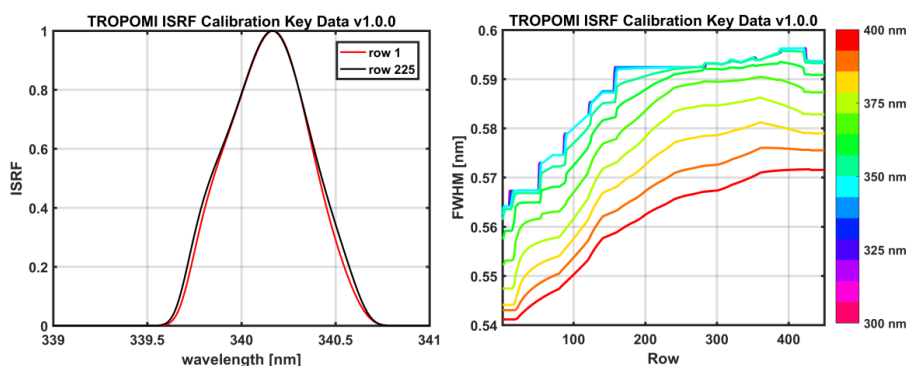
289 In a subsequent step of the processing, the absorption cross-sections of the different trace gases must be
290 convolved with the instrumental slit functions. The baseline approach is to use slit functions determined as part
291 of the TROPOMI key data. Slit functions, or Instrument Spectral Response Functions (ISRF), are delivered for
292 each binned spectrum and as a function of the wavelength as illustrated in Figure 5. Note that an additional
293 feature of the prototype algorithm allows to dynamically fit for an effective slit function of known line shape.
294 This can be used for verification and monitoring purpose during commissioning and later on during the mission.
295 This option is used for the QA4ECV OMI HCHO product.

296 More specifically, wavelength calibrations are made for each orbit as follows:

- 297 • The irradiances (one for each binned row of the CCD) are calibrated in wavelength over the 325-360
298 nm wavelength range, using 5 sub-windows.



- 299
- The earthshine radiances are first interpolated on the original L1 irradiance grid. The irradiance calibrated wavelength grid is assigned to those interpolated radiance values.
- 300
- The absorption cross-sections are interpolated (cubic spline interpolation) on the calibrated wavelength grid, prior to the analysis.
- 301
- In the case where averaged radiances are used as reference, an additional step must be performed: the cross-sections are aligned to the reference spectrum by means of shift/stretch values derived from a least-squares fit of the calibrated irradiance towards the averaged reference radiance.
- 302
- During spectral fitting, shift and stretch parameters for the radiance are derived, to align each radiance with cross sections and reference spectrum.
- 303
- 304
- 305
- 306
- 307



308

309 **Figure 5: Right panel: Examples of TROPOMI slit functions around 340 nm, for row 1 and row 225.**
310 **Left panel: TROPOMI spectral resolution in channel 3, as a function of the row and the wavelength,**
311 **derived from the instrument key data ISFR v1.0.0.**

312

313 Spike removal algorithm

314 A method to remove individual hot pixels or pixels affected by the South Atlantic Anomaly has been presented
315 for NO₂ retrievals in Richter et al. (2011). Often only a few individual detector pixels are affected and in these
316 cases, it is possible to identify and remove the outliers from the fit. However, as the amplitude of the distortion
317 is usually only of the order of a few percent or less, it cannot always be found in the highly structured spectra
318 themselves. Higher sensitivity for spikes can be achieved by analysing the residual of the fit where the
319 contribution of the Fraunhofer lines, scattering, and absorption is already removed. When the residual for a
320 single pixel exceeds the average residual of all pixels by a chosen threshold ratio (the tolerance factor), the
321 pixel is excluded from the analysis, in an iterative process. This procedure is repeated until no further outliers
322 are identified, or until the maximum number of iterations is reached (here fixed to 3). Tests performed with
323 OMI spectra show that a tolerance factor of 5 improves the HCHO fits. This is especially important to handle
324 the sensitivity of 2-D detector arrays to high energy particles. However, this improvement of the algorithm has
325 a non-negligible impact on the time of processing (x 1.8). This option is activated in the QA4ECV algorithm,
326 and will be activated in the TROPOMI operational algorithm in the next update of the processor.



327 2.2.2 Tropospheric air mass factor

328 In the DOAS approach, an optically thin atmosphere is assumed. The mean optical path of scattered photons
 329 can therefore be considered as independent of the wavelength within the relatively small spectral interval
 330 selected for the fit. One can therefore define a single effective air mass factor given by the ratio of the slant to
 331 the vertical optical depth of a particular absorber j :

$$M_j = \frac{\tau_{s,j}}{\tau_{v,j}}. \quad (6)$$

332 In the troposphere, scattering by air molecules, clouds and aerosols leads to complex light paths and therefore
 333 complex altitude-dependent air mass factors. Full multiple scattering calculations are required for the
 334 determination of the air mass factors, and the vertical distribution of the absorber has to be assumed *a priori*.
 335 For optically thin absorbers, the formulation of Palmer et al. (2001) is conveniently used. It decouples the
 336 height-dependent measurement sensitivity from the vertical profile shape of the species of interest, so that the
 337 tropospheric AMF (M) can be expressed as the average of the altitude dependent air mass factors (m_l) weighted
 338 by the partial columns (n_{al}) of the a priori vertical profile in each vertical layer l , from the surface up to the
 339 tropopause index (lt):

$$M = \frac{\sum_{l=1}^{lt} m_l(\lambda, \theta_0, \theta, \varphi, A_s, p_s, f_c, A_{cloud}, p_{cloud}) n_{al}(lat, long, time)}{\sum_{l=1}^{lt} n_{al}(lat, long, time)}, \quad (7)$$

340 where A_s is the surface albedo, p_s is the surface pressure, and f_c , A_{cloud} and p_{cloud} are respectively the cloud
 341 fraction, cloud albedo and cloud top pressure.

342 The altitude dependent air mass factors represent the sensitivity of the slant column to a change of the partial
 343 columns $N_{v,j}$ at a certain level. In a scattering atmosphere, m_l depends on the wavelength, the viewing angles,
 344 the surface albedo, and the surface pressure, but not on the partial column amounts or the vertical distribution
 345 of the considered absorber (optically thin approximation).

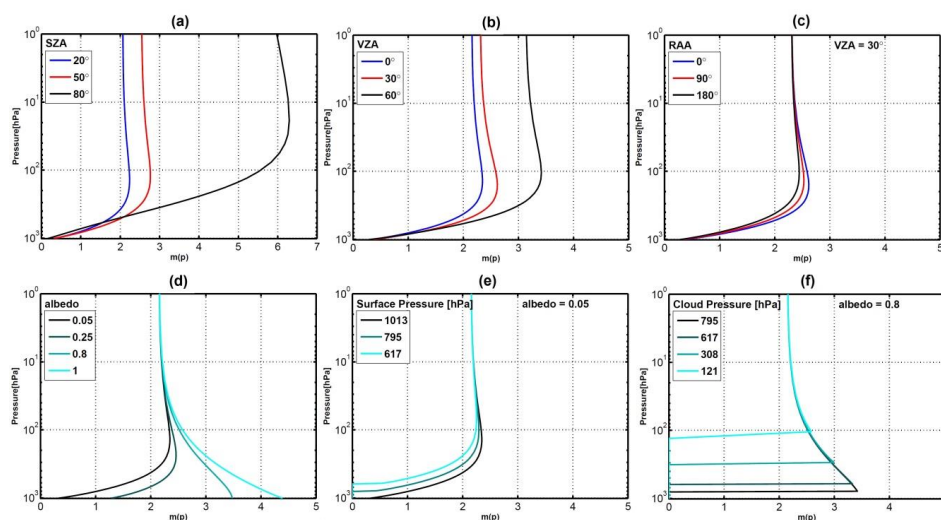
346 LUT of altitude dependent air mass factors

347 Generally speaking, m depends on the wavelength, as scattering and absorption processes vary with
 348 wavelength. However, in the case of HCHO, the amplitude of the M variation is found to be small (less than
 349 5% for SZA lower than 70°) in the 328.5-346 nm fitting window and a single air mass factor representative for
 350 the entire wavelength interval is used at 340 nm (Lorente et al., 2017).

351 Figure 6 illustrates the dependency of m with the observation angles, *i.e.* θ_0 (a), θ (b), and φ (c), and with scene
 352 conditions like A_s (d) and p_s for a weakly (e) or highly reflecting surface (f). The decrease of sensitivity in the
 353 boundary layer is more important for large solar zenith angles and wide instrumental viewing zenith angles.
 354 The relative azimuth angle does have relatively less impact on the measurement sensitivity (note however that
 355 aerosols and BRDF effects are not included in those simulations). In the UV, surfaces not covered with snow
 356 have an albedo lower than 0.1, while snow and clouds generally present larger albedos. For a weakly reflecting



357 surface, the sensitivity decreases near the ground because photons are mainly scattered, and scattering can take
 358 place at varying altitudes. Larger values of the surface albedo increase the fraction of reflected compared to
 359 scattered photons, increasing measurement sensitivity to tropospheric absorbers near the surface. Over snow
 360 or ice also multiple scattering can play an important role further increasing the sensitivity close to the surface.



361

362 **Figure 6: Variation of the altitude dependent air mass factor with: (a) solar zenith angle, (b) viewing**
 363 **zenith angle, (c) relative azimuth angle between the sun and the satellite, (d) surface albedo, (e) surface**
 364 **pressure for a weakly reflecting surface, (f) surface pressure for a highly reflecting surface. Unless**
 365 **specified, the parameters chosen for the radiative transfer simulations are: SZA=30°, VZA=0°, RAA=0°, albedo=0.05,**
 366 **surface pressure=1063hPa, $\lambda=340\text{nm}$.**

367 Altitude dependent air mass factors are calculated with the VLIDORT v2.6 radiative transfer model (Spurr,
 368 2008), at 340 nm, using an US standard atmosphere, for a number of representative viewing geometries, surface
 369 albedos and surface pressures (used both for ground and cloud surface pressures), and stored in a look-up table.
 370 Altitude dependent air mass factors are then interpolated within the lookup table for each particular observation
 371 condition and interpolated vertically on the pressure grid of the a priori profile, defined within the TM5-MP
 372 model (Williams et al., 2017). Linear interpolations are performed in $\cos(\theta_0)$, $\cos(\theta)$, relative azimuth angle
 373 and surface albedo, while a nearest neighbour interpolation is performed in surface pressure. The parameter
 374 values chosen for the look-up table are detailed in Table 4. In particular, the grid of surface pressure is very
 375 thin near the ground, in order to minimise interpolation errors caused by the generally low albedo of ground
 376 surfaces. Indeed, as illustrated by Figure 6 (e) and (f), the variation of the altitude dependent air mass factors
 377 is more discontinuous with surface elevation (low reflectivity) than with cloud altitude (high reflectivity).
 378 Furthermore, the LUT and model pressures are scaled to their respective surface pressures, in order to avoid
 379 extrapolations outside the LUT range.



380 **Table 4: Parameters in the altitude dependent air mass factors lookup table**

Parameter name	Nb. of grid points	Grid of values	Symbol
Solar zenith angle [°]	17	0, 10, 20, 30, 40, 45, 50, 55, 60, 65, 70, 72, 74, 76, 78, 80, 85	θ_0
Line of sight zenith angle [°]	10	0, 10, 20, 30, 40, 50, 60, 65, 70, 75	θ
Relative azimuth angle [°]	5	0, 45, 90, 135, 180	φ
Surface albedo	14	0, 0.01, 0.025, 0.05, 0.075, 0.1, 0.15, 0.2, 0.25, 0.3 0.4, 0.6, 0.8, 1.0	A_s
Surface pressure [hPa]	17	1063.10, 1037.90, 1013.30, 989.28, 965.83, 920.58, 876.98, 834.99, 795.01, 701.21, 616.60, 540.48, 411.05, 308.00, 226.99, 165.79, 121.11	p_s
Atmospheric pressure [hPa]	64	1056.77, 1044.17, 1031.72, 1019.41, 1007.26, 995.25, 983.38, 971.66, 960.07, 948.62, 937.31, 926.14, 915.09, 904.18, 887.87, 866.35, 845.39, 824.87, 804.88, 785.15, 765.68, 746.70, 728.18, 710.12, 692.31, 674.73, 657.60, 640.90, 624.63, 608.58, 592.75, 577.34, 562.32, 547.70, 522.83, 488.67, 456.36, 425.80, 396.93, 369.66, 343.94, 319.68, 296.84, 275.34, 245.99, 210.49, 179.89, 153.74, 131.40, 104.80, 76.59, 55.98, 40.98, 30.08, 18.73, 8.86, 4.31, 2.18, 1.14, 0.51, 0.14, 0.03, 0.01, 0.001	p_t
Altitude corresponding to the atmospheric pressure, using an US standard atmosphere [km] (for information)	64	-0.35, -0.25, -0.15, -0.05, 0.05, 0.15, 0.25, 0.35, 0.45, 0.55, 0.65, 0.75, 0.85, 0.95, 1.10, 1.30, 1.50, 1.70, 1.90, 2.10, 2.30, 2.50, 2.70, 2.90, 3.10, 3.30, 3.50, 3.70, 3.90, 4.10, 4.30, 4.50, 4.70, 4.90, 5.25, 5.75, 6.25, 6.75, 7.25, 7.75, 8.25, 8.75, 9.25, 9.75, 10.50, 11.50, 12.50, 13.50, 14.50, 16.00, 18.00, 20.00, 22.00, 24.00, 27.50, 32.50, 37.50, 42.50, 47.50, 55.00, 65.00, 75.00, 85.00, 95.00	z_t

381 **Treatment of partly cloudy scenes**

382 The AMF calculations for TROPOMI will use the cloud fraction (f_c), cloud albedo (A_{cloud}) and cloud pressure
 383 (p_{cloud}) from the S5P operational cloud retrieval, treating clouds as Lambertian reflectors (OCRA/ROCINN-
 384 CRB, Loyola et al., 2017). The applied cloud correction is based on the independent pixel approximation
 385 (Martin et al., 2002 and Boersma et al., 2004), in which a inhomogeneous satellite pixel is considered as a
 386 linear combination of two independent homogeneous scenes, one completely clear and the other completely
 387 cloudy. The intensity measured by the instrument for the entire scene is decomposed into the contributions
 388 from the clear-sky and cloudy fractions. Accordingly, for each vertical layer, the altitude dependent air mass



389 factor of a partly cloudy scene is a combination of two air mass factors, calculated respectively for the cloud-
 390 free and cloudy fractions of the scene:

$$m_l = (1 - w_c)m_{l_clear}(A_s, p_s) + w_cm_{l_cloud}(A_{cloud}, p_{cloud}) \quad (8)$$

391 where m_{l_clear} is the altitude dependent air mass factor for a completely cloud-free pixel, m_{l_cloud} is the altitude
 392 dependent air mass factor for a completely cloudy scene, and the cloud radiance fraction w_c is defined as:

$$w_c = \frac{f_c I_{cloud}(A_{cloud}, p_{cloud})}{(1 - f_c)I_{clear}(A_s, p_s) + f_c I_{cloud}(A_{cloud}, p_{cloud})} \quad (9)$$

393 I_{clear} and I_{cloud} are respectively the radiance intensities for clear-sky and cloudy scenes whose values are
 394 calculated with VLIDORT at 340 nm and stored in look-up tables with the same grids as the altitude dependent
 395 air mass factors. m_{l_clear} and I_{clear} are evaluated for a surface albedo A_s and a surface pressure p_s , while
 396 m_{l_cloud} and I_{cloud} are estimated for a cloud albedo A_{cloud} and at the cloud pressure p_{cloud} . Note that the
 397 variations of the cloud albedo are directly related to the cloud optical thickness. Strictly speaking in a
 398 Lambertian (reflective) cloud model approach, only thick clouds can be represented (one should keep in mind
 399 that still the penetration of photons into the cloud is not covered by the Lambertian model). An effective cloud
 400 fraction corresponding to an effective cloud albedo of 0.8 ($f_{eff} = f_c \frac{A_c}{0.8}$) can be defined, in order to transform
 401 optically thin clouds into equivalent optically thick clouds of reduced horizontal extent. In such altitude
 402 dependent air mass factor calculations, a single cloud top pressure is assumed within a given viewing scene.
 403 For low effective cloud fractions (f_{eff} lower than 10%), the cloud top pressure retrieval is generally highly
 404 unstable and it is therefore reasonable to consider the observation as a clear-sky pixel (i.e. the cloud fraction is
 405 set to 0) in order to avoid unnecessary error propagation through the retrievals. This 10% threshold might be
 406 adjusted according to the quality of the cloud product (Veefkind et al., 2016; Loyola et al., 2017).

407 It should be noted that this formulation of the altitude dependent air mass factor for a partly cloudy pixel
 408 implicitly includes a correction for the HCHO column lying below the cloud and therefore not seen by the
 409 satellite, the so-called “ghost column”. Indeed, the total AMF calculation as expressed by (7) and (8) assumes
 410 the same a priori vertical profile in both cloudy and clear parts of the pixel and implies an integration of the
 411 profile from the top of atmosphere to the ground, for each fraction of the scene. The ghost column information
 412 is thus coming from the a priori profiles. For this reason, observations with cloud fractions f_{eff} larger than
 413 30% are assigned with a poor quality flag and have to be used with caution.



414 **Aerosols**

415 The presence of aerosol in the observed scene may affect the quality of the retrieval. No explicit treatment of
 416 aerosols (absorbing or not) is foreseen in the operational algorithm as there is no general and easy way to treat
 417 the aerosols effect on the retrieval. At computing time, the aerosol parameters (extinction profile, single
 418 scattering albedo, ...) are unknown. However, the information on the AAI (Stein Zweers et al., 2016) will be
 419 included in the L2 HCHO files as it gives information to the user on the presence of absorbing aerosols and the
 420 affected data should be used and interpreted with care.

421 **A priori vertical profile shapes**

422 Formaldehyde concentrations decrease with altitude as a result of the near-surface sources of short-lived
 423 NMVOC precursors, the temperature dependence of CH₄ oxidation, and the altitude dependence of photolysis.
 424 The profile shape varies according to local NMHC sources, boundary layer depth, photochemical activity, and
 425 other factors.

426 To resolve this variability in the TROPOMI near-real time HCHO product, daily forecasts calculated with the
 427 TM5-MP chemical transport model (Huijnen et al., 2010, Williams et al., 2017) will be used to specify the
 428 vertical profile shape of the HCHO distribution. TM5-MP will also provide a priori profile shapes for the NO₂,
 429 SO₂, and CO retrievals. For the QA4ECV OMI products, high-resolution TM5-MP model runs were performed
 430 for the period 2004-2016, and the model profiles from this run are used for both HCHO and NO₂ retrievals.

431 TM5-MP is operated with a spatial resolution of 1°x1° in latitude and longitude, and with 34 sigma pressure
 432 levels up to 0.1hPa in the vertical direction. TM5-MP uses 3-hourly meteorological fields from the European
 433 Centre for Medium Range Weather Forecast (ECMWF) operational model (ERA-Interim reanalysis data for
 434 reprocessing, and the operational archive for real time applications and forecasts). These fields include global
 435 distributions of wind, temperature, surface pressure, humidity, and (liquid and ice) water content, and
 436 precipitation.

437 For the calculation of the HCHO air mass factors, the profiles are linearly interpolated in space and time, at
 438 pixel centre and local overpass time, through a model time step of 30 minutes. To reduce the errors associated
 439 to topography and the lower spatial resolution of the model compared to the TROPOMI 3.5x7 km² spatial
 440 resolution, the a priori profiles need to be rescaled to effective surface elevation of the satellite pixel. Following
 441 Zhou et al. (2009) and Boersma et al (2011), the TM5-MP surface pressure is converted by applying the
 442 hypsometric equation and the assumption that the temperature changes linearly with height:

$$p_s = p_{s, TM5} \left(\frac{T_{TM5}}{T_{TM5} + \Gamma(z_{TM5} - z_s)} \right)^{\frac{g}{RT}} \quad (10)$$

443 Where $p_{s, TM5}$ and T_{TM5} are the TM5-MP surface pressure and temperature, $\Gamma = 0.0065 \text{K m}^{-1}$ the lapse rate,
 444 z_{TM5} the TM5-MP terrain height, and z_s surface elevation for the satellite ground pixel from a digital elevation



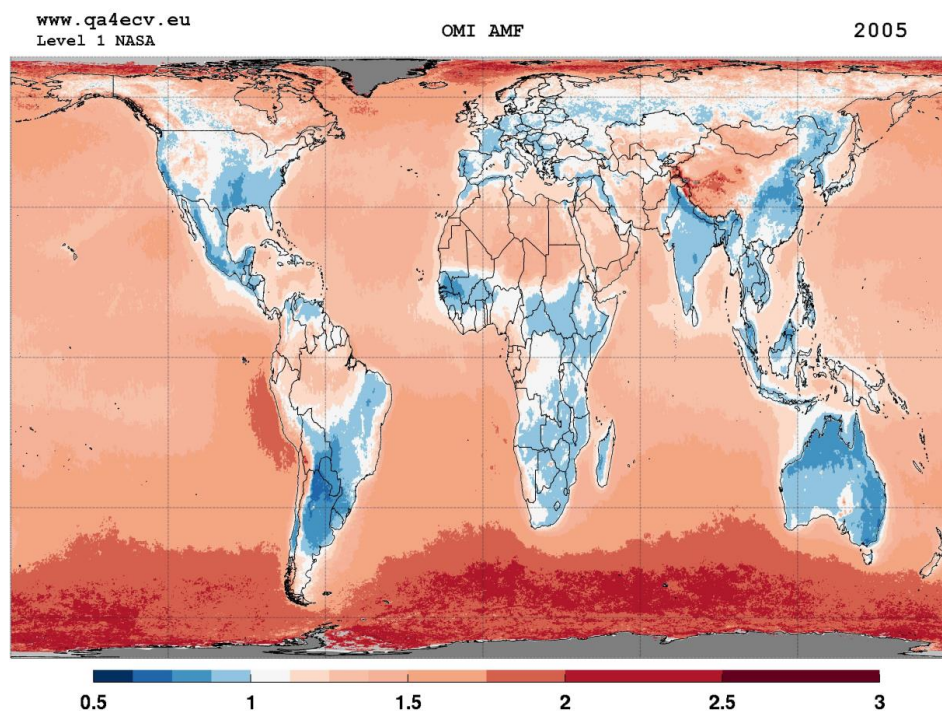
445 map at high resolution. $R=287 \text{ J kg}^{-1} \text{ K}^{-1}$ is the gas constant for dry air, and $g = 9.8 \text{ ms}^{-2}$ the gravitational
 446 acceleration.

447 The pressure levels for the a priori HCHO profiles are based on the improved surface pressure level p_s :
 448 $p_l = a_l + b_l p_s$, a_l and b_l being the constants that effectively define the vertical coordinate (Table 13).

449 Yearly averaged air mass factors obtained using prior information summarized in Table 5, in particular TM5-
 450 MP HCHO profiles, are presented in Figure 7, in order to give an overview of the tropospheric AMF values
 451 and their global regional variations.

452 **Table 5: Prior information datasets used in the air mass factor calculation in the S5P HCHO**
 453 **operational algorithm and in the QA4ECV OMI algorithm.**

Prior information	Origin of data set	Resolution	Symbol
Surface Albedo	OMI-based monthly minimum LER (update of Kleipool et al., 2008)	<ul style="list-style-type: none"> month $0.5^\circ \times 0.5^\circ$ (lat x long) 342 nm 	A_s
Digital elevation map	GMTED2010 (Danielson et al., 2011)	Average over the ground pixel area.	z_s
Cloud fraction	Operational cloud product based on a Lambertian cloud model (S5P: Loyola et al., 2017; OMI: Veeffkind et al., 2016).	For each ground pixel.	f_c
Cloud pressure			p_{cloud}
Cloud albedo			A_{cloud}
A priori HCHO profiles	Forecast (NRT) or reanalysis from TM5-MP CTM	<ul style="list-style-type: none"> Daily profiles at overpass time $1^\circ \times 1^\circ$ (lat x long) 34 sigma pressure levels up to 0.1hPa 	n_a



455 **Figure 7: Yearly averaged map of tropospheric air mass factors at 340 nm using the QA4ECV OMI**
456 **HCHO algorithm. A priori HCHO profiles from high-resolution TM5-MP model runs have been used.**
457 **The IPA cloud correction is applied for effective cloud fractions f_{eff} larger than 10%. Observations**
458 **with f_{eff} larger than 30% have been filtered out.**

459 2.2.3 Cross-track and zonal reference sector correction

460 Residual latitude-dependent biases in the columns, due to unresolved spectral interferences, are known to
461 remain a limiting factor for the retrieval of weak absorbers such as HCHO. Retrieved HCHO slant columns
462 can present large offsets depending on minor changes in the fit settings, and on minor instrumental spectral
463 inaccuracies. Resulting offsets are generally global but also show particular dependencies, mainly with detector
464 row (across-track) and with latitude (along-track). In the case of a 2D-detector array such as OMI or
465 TROPOMI, across-track striping can possibly arise, due to imperfect calibration and different dead/hot pixel
466 masks for the CCD detector regions. Offset corrections are also meant to handle some effects of the time-
467 dependent degradation of the instrument.

468 A large part of the resulting systematic HCHO slant column uncertainty is reduced by the application of a
469 background correction, which is based on the assumption that the background HCHO column observed over
470 remote oceanic regions (Pacific Ocean) is only due to methane oxidation. The natural background level of
471 HCHO is well estimated from chemistry model simulations of CH_4 oxidation ($N_{v,0,CTM}$). It is ranging from 2
472 to 4×10^{15} molec. cm^{-2} , depending on the latitude and the season (De Smedt et al., 2008; 2015; González Abad
473 et al., 2015).



474 For the HCHO retrieval algorithm, we use a 2-steps normalization of the slant columns (see Table 6):

- 475
- 476 • Across-track: the mean HCHO slant column is determined for each row in the reference sector around
 477 the equator $[-5^\circ 5^\circ]$, $[180^\circ 240^\circ]$. Data selection is based on the slant column errors from the DOAS
 478 fit and on the cloud fraction (threshold values are given in Table 6). Those mean HCHO values are
 479 subtracted from all the slant columns of the same day, as a function of the row. The aim is to reduce
 480 possible row-dependent offsets. In the case were solar irradiance are used as reference, those offsets
 481 can exceed 2×10^{16} molec.cm⁻². They are reduced below 10^{15} molec.cm⁻² by this first step, or when
 482 row averaged radiances are used as reference, as in the QA4ECV algorithm.
 - 483 • Along-track: the latitudinal dependency of the across-track corrected HCHO SCs is modelled by a
 484 polynomial fit through their mean values, all rows combined, in 5° latitude bins in the reference sector
 485 $([-90^\circ 90^\circ]$, $[180^\circ 240^\circ])$. Again, data selection is based on the slant column errors from the DOAS
 fit and on the cloud fraction.

486 These two corrections are applied to the global slant columns so that in the reference sector, the mean
 487 background corrected slant columns ($\Delta N_s = N_s - N_{s,0}$) are centered around zero.

488 **Table 6: 2-steps normalization of the HCHO vertical columns**

Correction	Region	Time frame	Column correction	Observation selection
Across-track	Equatorial Pacific Lat: $[-5^\circ 5^\circ]$, Long: $[180^\circ 240^\circ]$	NRT: 1-week moving window	$dN_s(\text{row}) = N_s(\text{row}) - \overline{N_{s,0}(\text{row})}$	$\sigma_{N_s} \leq 3\overline{\sigma_{N_s}}$ $f_c \leq 0.4$
Zonal Along-track	Pacific Lat: $[-90^\circ 90^\circ]$, Long: $[180^\circ 240^\circ]$	Offline: Daily correction	$\Delta N_s(\text{lat}) = dN_s(\text{lat}) - \overline{dN_{s,0}(\text{lat})}$ $\overline{N_{s,0,CTM}(\text{lat})} = \overline{M_0(\text{lat})N_{v,0,CTM}(\text{lat})}$	$\overline{dN_{s,0}(\text{lat})}$ $\leq 5e16$

489 To the corrected slant columns, the background HCHO values from a model have to be added. A latitude-
 490 dependent polynomial is fitted daily through 5° latitude bin means of those modelled values in the reference
 491 sector. Corresponding values are added to all the columns of the day. Strictly speaking, those background
 492 values should be slant columns, derived as the product of air mass factors in the reference sector (M_0) with
 493 HCHO vertical columns from the model ($N_{s,0,CTM} = M_0 N_{v,0,CTM}$) (González Abad et al., 2015). However, this
 494 option requires the storage of the slant columns, the air mass factors, and their errors, in a separated database
 495 (QA4ECV Algorithm and SSP option, see Equation (11)). An approximate solution is to add as background
 496 the constant vertical column from the model ($N_{v,0,CTM}$), hence neglecting the variability of the M_0/M ratio. This
 497 is the current implementation in the SSP algorithm, which will be updated with equation (11) after launch. For
 498 NRT purpose, the evaluation in the reference sector is made using a moving time window of 1 week. For offline
 499 processing, the reference sector correction can be refined by using daily evaluations.

$$N_v = \frac{N_s - N_{s,0}}{M} + N_{v,0} = \frac{\Delta N_s}{M} + \frac{M_0}{M} N_{v,0,CTM} = \frac{\Delta N_s + N_{s,0,CTM}}{M} \quad (11)$$



500 Figure 3 presents some examples of monthly and regionally averaged vertical columns, together with the
 501 contribution of $N_{v,0}$. It should be realized that this contribution accounts for 20 to 50% of the vertical columns,
 502 as expected from the large contribution of methane oxidation to the total HCHO column (Stavrakou et al.,
 503 2015).

504 3. Uncertainty analyses

505 3.1 Uncertainty formulation by uncertainty propagation

506 The total uncertainty on the HCHO vertical column is composed of many sources of (random and systematic)
 507 errors. In part those are related to the measuring instrument, such as errors due to noise or knowledge of the
 508 slit function. In a DOAS-type algorithm, those instrumental errors propagate into the uncertainty of the slant
 509 columns. Other types of error can be considered as model errors and are related to the representation of the
 510 observation physical properties that are not measured. Examples of model errors are uncertainties on the trace
 511 gas absorption cross-sections, the treatment of clouds and uncertainties of the a priori profiles. Model errors
 512 can affect the slant columns, the air mass factors or the applied background corrections.

513 A formulation of the uncertainty can be derived analytically by error propagation, starting from the equation
 514 of the vertical column (11) which directly results from the different retrieval steps. As the main algorithm steps
 515 are performed independently, they are assumed to be uncorrelated. The total uncertainty on the tropospheric
 516 vertical column can be expressed as (Boersma et al., 2004, De Smedt et al., 2008):

$$\sigma_{N,v}^2 = \left(\frac{\partial N_v}{\partial N_s} \sigma_{N,s}\right)^2 + \left(\frac{\partial N_v}{\partial M} \sigma_M\right)^2 + \left(\frac{\partial N_v}{\partial N_{s,0}} \sigma_{N,s,0}\right)^2 + \left(\frac{\partial N_v}{\partial M_0} \sigma_{M,0}\right)^2 + \left(\frac{\partial N_v}{\partial N_{v,0,CTM}} \sigma_{N,v,0,CTM}\right)^2 \quad (12)$$

$$\sigma_{N,v}^2 = \frac{1}{M^2} \left(\sigma_{N,s}^2 + \frac{(\Delta N_s + M_0 N_{v,0,CTM})^2}{M^2} \sigma_M^2 + \sigma_{N,s,0}^2 + N_{v,0,CTM}^2 \sigma_{M,0}^2 + M_0^2 \sigma_{N,v,0,CTM}^2 \right) \quad (13)$$

517 where $\sigma_{N,s}$, σ_M , $\sigma_{N,s,0}$, $\sigma_{M,0}$ and $\sigma_{N,v,0,CTM}$ are respectively the errors on the slant column, the air mass factor,
 518 and the slant column correction, the air mass factor, and the model vertical column in the reference sector
 519 (indicated by suffix 0). For each of these categories, the following sections provide more details on the
 520 implementation of the uncertainty estimate in the HCHO algorithm. A discussion of the sources of uncertainties
 521 and, where possible, their estimated size are presented, as well as their spatial and temporal patterns.

522 Note that in the current implementation of the operational processor, $M_0 = M$, and the uncertainty formulation
 523 therefore reduces to:



$$\sigma_{N,v}^2 = \frac{1}{M^2} \left(\sigma_{N,s}^2 + \frac{\Delta N_s^2}{M^2} \sigma_M^2 + \sigma_{N,s,0}^2 \right) + \sigma_{N,v,0,CTM}^2 \quad (14)$$

524 Complementing this error propagation analysis, total column averaging kernels (A) based on the formulation
 525 of Eskes and Boersma (2003) are estimated. Column averaging kernels provide essential information when
 526 comparing measured columns with e.g. model simulations or correlative validation data sets, because they
 527 allow removing the effect of the a-priori HCHO profile shape used in the retrieval (see APPENDIX C:
 528 Averaging Kernel, Boersma et al., 2004; 2016).

529 Section 3.2 presents our current estimates of the precision (random uncertainty) and the trueness (systematic
 530 uncertainty) that can be expected for the TROPOMI HCHO vertical columns. They are discussed along with
 531 the product requirements (Section 2.1).

532 3.1.1 Errors on the slant columns

533 Error sources that contribute to the total uncertainty on the slant column originate both from instrument
 534 characteristics and from uncertainties in the DOAS slant column fitting procedure itself.

535 The retrieval noise for individual observations is limited by the SNR of the spectrometer measurements. A
 536 good estimate of the random variance of the reflectance (which results from the combined noise of radiance
 537 and reference spectra) is given by the reduced χ^2 of the fit, which is defined as the sum of squares (4) divided
 538 by the number of degrees of freedom in the fit. The covariance matrix (Σ) of the linear least squares parameter
 539 estimate is then given by:

$$\Sigma = \frac{\chi^2}{(k-n)} (A^T A)^{-1} \quad (15)$$

540 where k is the number of spectral pixels in the fitting interval, n is the number of parameters to fit and the
 541 matrix $A(j \times k)$ is formed by the cross-sections. For each absorber j , the value $\sigma_{N,s,j}$ is usually called the slant
 542 column error (SCE or $\sigma_{N,s,rand}$).

$$\sigma_{N,s,j}^2 = \frac{\chi^2}{(k-n)} (A^T A)^{-1}_{j,j} \quad (16)$$

543 Equation (16) does not take into account systematic errors, that are mainly dominated by slit function and
 544 wavelength calibration uncertainties, absorption cross-section uncertainties, by interferences with other species
 545 (O_3 , BrO or O_4), or by uncorrected stray light effects. The choice of the retrieval interval can have a significant
 546 impact on the retrieved HCHO slant columns. The systematic contributions to the slant column errors are
 547 empirically estimated from sensitivity tests (see Table 7) and can be viewed as part of the structural uncertainty
 548 (Lorente et al., 2017). However, remaining systematic offsets and zonal biases are greatly reduced by the
 549 reference sector correction. All effects summed in quadrature, the various contributions are estimated to
 550 account for an additional systematic error of 20% of the background-corrected slant column:



$$\sigma_{N,s,sys} = 0.2\Delta N_s \quad (17)$$

551 The total error on slant columns is then:

$$\sigma_{N,s}^2 = \sigma_{N,s,rand}^2 + \sigma_{N,s,sys}^2 \quad (18)$$

552 **Table 7: Summary of the different error sources considered in the HCHO slant column uncertainty**
 553 **budget.**

Error source	Parameter uncertainty	Estimated uncertainty on HCHO SCD	Evaluation method - reference
Measurement noise	S/N=800-1000	1x10 ¹⁶ molec.cm ⁻² (random)	Value derived for individual observations by error propagation; De Smedt et al., 2015;
HCHO cross-section error	Based on alternative cross-section datasets, offset and polynomial orders.	9%	Mean values derived from sensitivity tests using GOME-2 and OMI data. De Smedt et al., 2008; 2015 Hewson et al., 2013 Pinardi et al., 2013
O ₃ cross-section error		5%	
BrO cross-section error		5%	
NO ₂ cross-section error		3%	
Ring correction error		5%	
Choice of offset order		7%	
Choice of polynomial order	7%		
Instrumental slit function and wavelength calibration	Based on alternative calibrations	10%	Mean value derived from sensitivity tests using GOME-2 and OMI data.
Choice of wavelength interval	Based on alternative wavelength intervals	10%	Mean value derived from sensitivity tests using GOME-2 and OMI data. Hewson et al., 2013
Temperature dependence of the HCHO XS	0.05%/°K	2%	Mean value derived from sensitivity tests based on Meller and Moorgat (2000)

554 3.1.2 Errors on air mass factors

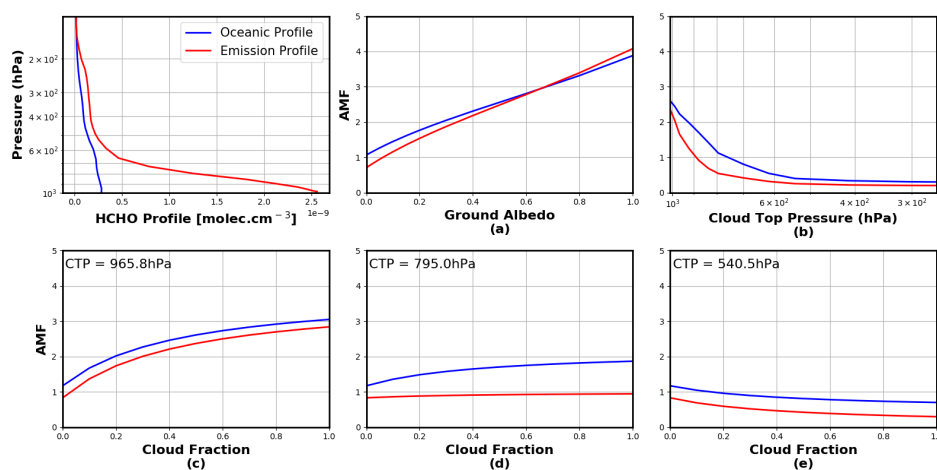
555 The errors on the air mass factor depend on input parameter uncertainties and on the sensitivity of the air mass
 556 factor to each of them. This contribution is broken down into the squared sum (Boersma et al., 2004, De Smedt
 557 et al., 2008):

$$\sigma_M^2 = \left(\frac{\partial M}{\partial A_s} \cdot \sigma_{A,s}\right)^2 + \left(\frac{\partial M}{\partial f_c} \cdot \sigma_{f,c}\right)^2 + \left(\frac{\partial M}{\partial p_{cloud}} \cdot \sigma_{p,cloud}\right)^2 + \left(\frac{\partial M}{\partial s} \cdot \sigma_s\right)^2 + (0.2M)^2 \quad (19)$$

558 The contribution of each parameter to the total air mass factor error depends on the observation conditions.
 559 The air mass factor sensitivities ($M' = \frac{\partial M}{\partial parameter}$), i.e. the air mass factor derivatives with respect to the
 560 different input parameters, can be derived for any particular condition of observation using the altitude-
 561 dependent AMF LUT, and using the model profile shapes (see Figure 8). In practice, a LUT of AMF
 562 sensitivities has been created using coarser grids than the AMF LUT, and one parameter describing the shape



563 of the profile: the profile height, i.e. the altitude (pressure) below which resides 75% of the integrated HCHO
 564 profile. $\frac{\partial M}{\partial s}$ is approached by $\frac{\partial M}{\partial s_h}$ where s_h is half of the profile height. Relatively small variations of this
 565 parameter have a strong impact on the total air mass factors, because altitude-resolved air mass factors decrease
 566 quickly in the lower troposphere, where the HCHO profiles peak (Figure 6).



567

568 **Figure 8: First panel: TM5-MP HCHO profiles extracted in June over the equatorial Pacific ocean**
 569 **and over Beijing (red). Those profiles have been used to calculate the tropospheric air mass**
 570 **factors shown in the panels a to e, representing the AMF dependence on (a) the surface albedo, (b) the**
 571 **cloud altitude, (c), (d), (e) the cloud fraction. In all cases, we consider a nadir view and a solar zenith**
 572 **angle of 30°. In (a) the pixel is cloud free, in (b) the albedo is 0.02 and the effective cloud fraction is 0.5,**
 573 **in (c), (d), (e) the ground albedo is 0.02 and the cloud pressure is respectively 966, 795 and 540 hPa.**

574 The errors $\sigma_{A,s}$, $\sigma_{f,c}$, $\sigma_{p,cloud}$, $\sigma_{s,h}$ are typical uncertainties on the surface albedo, cloud fraction, cloud top
 575 pressure and profile shape, respectively. They are estimated from the literature or derived from comparisons
 576 with independent data (see Table 8). Together with the sensitivity coefficients, these give the first four
 577 contributions on the right of equation (19). The fifth term on the right of equation (19) represents the uncertainty
 578 contribution due to possible errors in the AMF model itself (Lorente et al., 2017). We estimate this contribution
 579 to 20% of the air mass factor (see also section 3.2.2).

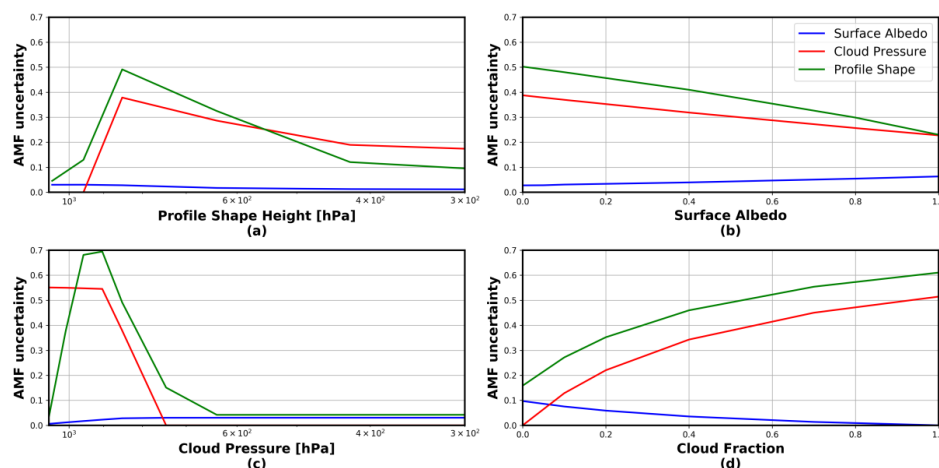
580 Estimates of the air mass factor uncertainties and of their impact on the vertical column uncertainties are listed
 581 in Table 8 and represented in Figure 9. They are based on the application of equation (19) to HCHO columns
 582 retrieved from OMI measurements. In expression (19), the impact of possible correlations between
 583 uncertainties on parameters is not considered, like for example the surface albedo and the cloud top pressure.
 584 Note also that errors on the solar angles, the viewing angles and the surface pressure are supposed to be
 585 negligible, which is not totally true in practice, since equation (10) does not yield the true surface pressure but
 586 only a good approximation.



587 **Table 8: Summary of the different error sources considered in the air mass factor uncertainty budget.**

Input parameter error	Symbol	Parameter Uncertainty	Source	Estimated uncertainty on HCHO VCD
Surface albedo	σ_{A_s}	0.02	Kleipool et al., 2008	10-20%
Cloud fraction	$\sigma_{f,c}$	0.05	Veefkind et al., 2016	05-15%
Cloud height	$\sigma_{p,cloud}$	50hPa		10-20%
Profile shape height	σ_s	100hPa	Upper limit of TM5-MP profile height standard deviation.	20-60%
AMF wavelength dependency	Model / Structural uncertainty	20%	Lorente et al., 2017	15-35%
LUT interp. errors				
Model atmosphere				
Cloud model/cloud correction/				
No explicit aerosol correction				

588



589

590 **Figure 9: AMF uncertainty related to profile shape, cloud pressure and surface albedo errors, as a**
 591 **function of different observation conditions.**

592

593 **Surface albedo**

594 A reasonable uncertainty on the albedo is 0.02 (Kleipool et al., 2008). This translates to an error on the air mass
 595 factor using the slope of the air mass factor as a function of the albedo and can be evaluated for each satellite
 596 pixel (equation (19)). As an illustration, Figure 8 (a) shows the air mass factor dependence on the ground albedo
 597 for two typical HCHO profile shapes (in blue: remote profile, in red: emission profile). At 340nm, the AMF



598 sensitivity (the slope), is almost constant with albedo, being only slightly higher for low albedo values. As
599 expected, the AMF sensitivity to albedo is higher for an emission profile peaking near the surface than for a
600 background profile more spread in altitude. More substantial errors can be introduced if the real albedo differs
601 considerably from what is expected, for example in the case of the sudden snowfall or ice cover. Snow/ice
602 cover map will therefore be used for flagging such cases.

603 **Clouds and aerosols**

604 An uncertainty on the cloud fraction of 0.05 is considered, while an uncertainty on the cloud top pressure of
605 50hPa is taken. Figure 8 (b) shows the air mass factor variation with cloud altitude. The AMF is very sensitive
606 to the cloud top pressure (the slope is steepest) when the cloud is located below or at the level of the
607 formaldehyde peak. For higher clouds, the sensitivity of the air mass factor to any change in cloud pressure is
608 very weak. As illustrated in Figure 8 (c), (d) and (e), for which a cloud top pressure of 966, 795 and 540 hPa
609 is respectively considered, the sensitivity to the cloud fraction is mostly significant when the cloud lies below
610 the HCHO layer.

611 The effect of aerosols on the air mass factors are not explicitly considered in the HCHO retrieval algorithm.
612 To a large extent, however, the effect of the non-absorbing part of the aerosol extinction is implicitly included
613 in the cloud correction (Boersma et al., 2011). Indeed, in the presence of aerosols, the cloud detection algorithm
614 is expected to overestimate the cloud fraction. Since non-absorbing aerosols and clouds have similar effects on
615 the radiation in the UV-visible range, the omission of aerosols is partly compensated by the overestimation of
616 the cloud fraction, and the resulting error on air mass factor is small, typically below 15% (Millet et al., 2006;
617 Boersma et al., 2011; Lin et al., 2014; Castellanos et al., 2015; Chimot et al. 2015). In some cases, however,
618 the effect of clouds and aerosols will be different. For example, when the cloud height is significantly above
619 the aerosol layer, clouds will have a shielding effect while the aerosol amplifies the signal through multiple
620 scattering. This will result in an underestimation of the AMF. Absorbing aerosols have also a different effect
621 on the air mass factors, since they tend to decrease the sensitivity to HCHO concentration. In this case, the
622 resulting error on the air mass factor can be as high as 30% (Palmer et al., 2001; Martin et al., 2002). This may,
623 for example, affect significantly the derivation of HCHO columns in regions dominated by biomass burning
624 as well as over heavily industrialized regions. Shielding and reflecting effect can thus occur, depending on the
625 observation, decreasing or increasing the sensitivity to trace gas absorption. It has been shown that uncertainties
626 related to aerosols is reduced by spatiotemporal averaging (Barkley et al., 2012; Lin et al., 2014; Castellanos
627 et al., 2015; Chimot et al. 2015). Furthermore, the applied cloud filtering effectively removes observations with
628 the largest aerosol optical depth. In the HCHO product, observations with an elevated absorbing aerosol index
629 will be flagged, to be used with caution.

630

631 **Profile shape**

632 This contribution to the total AMF error is the largest when considering monthly averaged observations. This
633 is supported by validation results using MAX-DOAS profiles measured around Beijing and Wuxi (see De
634 Smedt et al. 2015, Wang et al., 2016). Taking into account the averaging kernels allows removing from the



635 comparison the error related to the a priori profiles, when validating the results against other modelled or
 636 measured profiles (see the APPENDIX C: Averaging Kernel).

637 3.1.3 Errors on the reference sector correction

638

$$\sigma_{N,v,0}^2 = \frac{1}{M^2} (\sigma_{N,s,0}^2 + N_{v,0,CTM}^2 \sigma_{M,0}^2 + M_0^2 \sigma_{N,v,0,CTM}^2) \quad (20)$$

639 This error includes contributions from the model background vertical column, from the error on the air mass
 640 factor in the reference sector, and from the amplitude of the normalization applied to the HCHO columns. As
 641 mentioned in 3.1.1, we consider that $\sigma_{N,s,0}$ is taken into account in Equation (17). The error on the air mass
 642 factor in the reference sector $\sigma_{M,0}$ is calculated as in Equation (20) and saved during the background correction
 643 step. Uncertainty on the model background has been estimated as the monthly averaged differences between
 644 two different CTM simulations in the reference sector: IMAGES (Stavrakou et al., 2009a) and TM5-MP
 645 (Huijnen et al., 2010). The differences range between 0.5 and 1.5×10^{15} molec.cm⁻².

646 **Table 9: Estimated errors on the reference sector correction.**

Error source	Uncertainty on HCHO VCD	Evaluation method – reference
Model background	0.5 and 1.5×10^{15} molec.cm ⁻²	Difference between IMAGES and TM model
Amplitude of the column normalisation ($N_{s,0}$)	0 to 4×10^{15} molec.cm ⁻²	Sensitivity tests using GOME-2 and OMI data.

647 3.2 HCHO error estimates and product requirements

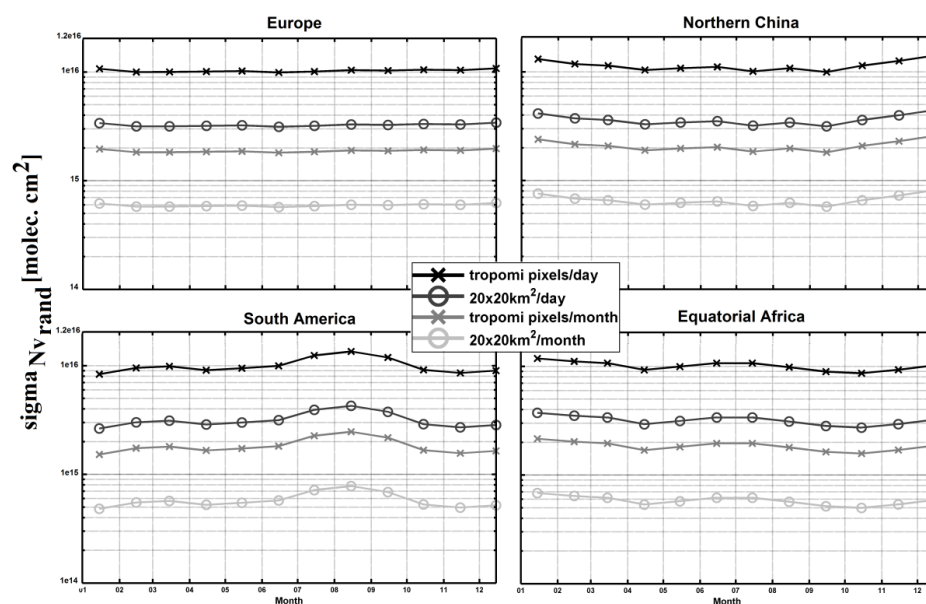
648 This section presents estimates of the precision (random error) and trueness (systematic error) that can be
 649 expected for the TROPOMI HCHO vertical columns. These estimates are given in different NMVOC emission
 650 regions. Precision and trueness of the HCHO product are discussed against the user requirements.

651 3.2.1 Precision

652 When considering individual pixels, the total uncertainty is dominated by the random error on the slant
 653 columns. Our simulations and tests on real satellite measurements show that the precision by which the HCHO
 654 can be measured is well defined by the instrument signal-to-noise level. For the nominal SNR level (1000), the
 655 expected precision of single-pixel measurements is equivalent to the precision obtained with OMI HCHO
 656 retrievals (De Smedt et al., 2015), but with a ground pixel size of about 3.5×7 km², i.e. one order of magnitude
 657 smaller in surface. Absolute $\sigma_{N,s,rand}$ values typically range between 7 and 12×10^{15} molec.cm⁻² for individual
 658 pixels, showing an increase as a function of the surface altitude and of the solar zenith angle. Relative values
 659 range between 100 and 300%, depending on the observation scene. In the case of HCHO retrievals, for
 660 individual satellite ground pixels, the random uncertainty on the slant columns is the most important source of
 661 uncertainty on the total vertical column. It can be reduced by averaging the observations, but of course at the
 662 expense of a loss in time and/or spatial resolution.



663 The precision of the vertical columns provided in the L2 files corresponds to the precision of the slant column
 664 divided by the air mass factor
 665 $\sigma_{N,v,rand} = \frac{\sigma_{N,s,rand}}{M}$ (see Table 13). It is dependent on the air mass factors, and therefore on the observation
 666 conditions and on the cloud statistics. Figure 10 shows the vertical column precision that is expected for
 667 TROPOMI, based on OMI observations in 2005. Results are shown in several regions, and at different spatial
 668 and temporal scales (from individual pixels to monthly averaged column in 20x20km² grids). The product
 669 requirements for HCHO measurements state a precision of 1.3x10¹⁵ molec.cm⁻². This particular requirement
 670 cannot be achieved with individual observations at full spatial resolution. However, as represented in Figure
 671 10, the requirement can be approached using daily observations at the spatial resolution of 20x20km² (close to
 672 the OMI resolution) or using monthly averaged columns at the TROPOMI resolution. The precision can be
 673 brought below 1x10¹⁵ molec.cm⁻² if a spatial resolution of 20x20km² is considered for monthly averaged
 674 columns.



675

676 **Figure 10: Estimated precision on the TROPOMI HCHO columns, in several NMVOC emission**
 677 **regions, and at different spatial and temporal scales (from individual pixels to monthly averages in**
 678 **20x20 km² grids). These estimated are based on OMI observations in 2005, using observations with an**
 679 **effective cloud fraction lower than 40%.**

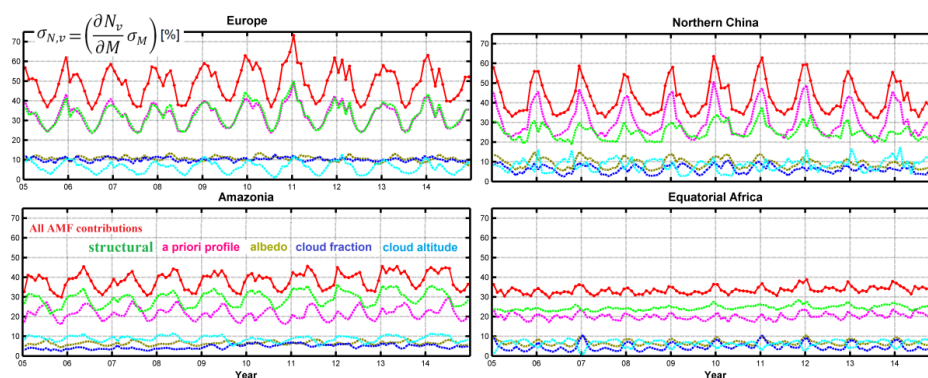
680 3.2.2 Trueness

681 In this section, we present monthly averaged values of the systematic vertical columns uncertainties estimated
 682 for OMI retrievals between 2005 and 2014. The contribution of the air mass factor uncertainties is the largest
 683 contribution to the vertical column systematic uncertainties (see also Table 10). Figure 11 presents the VCD
 684 uncertainties due to AMF errors, and the five considered contributions, over Equatorial Africa and Northern
 685 China, as example of Tropical and mid-latitude sites. The largest contributions are from the a priori profile



686 uncertainty and from the structural uncertainty (taken as 20% of the AMF). In the case where the satellite
 687 averaging kernels are used for comparisons with external HCHO columns, the a priori profile contribution can
 688 be removed from the comparison uncertainty budget, leading to a total uncertainty in the range of 25% to 50%.
 689 Table 10 wraps up the estimated relative contributions to the HCHO vertical column uncertainty, in the case
 690 of monthly averaged columns for typical low and high columns.

691 Considering these estimates of the HCHO column trueness, the requirements for HCHO product (30%) are
 692 achievable in regions of high emissions and for certain times of the year. In any case, observations need to be
 693 averaged to reduce random uncertainties at a level comparable or smaller than systematic uncertainties.



694

695 **Figure 11: Regional and monthly average of the relative systematic vertical column AMF-related**
 696 **uncertainties in several NMVOC emission regions, for the period 2005-2014. The 5 contributions to the**
 697 **systematic air mass factor uncertainty are shown: structural (green), a priori profile (pink), albedo**
 698 **(olive), cloud fraction (blue) and cloud altitude (cyan).**

699 **Table 10: Estimated HCHO vertical column uncertainty budget for monthly averaged low and**
 700 **elevated columns (higher than 1×10^{16} molec.cm⁻²). Contributions from the three retrieval steps are**
 701 **provided, as well as input parameter contributions.**

HCHO vertical error uncertainty	Remote regions / low columns	Elevated column regions / periods
Contribution from systematic slant columns uncertainties	25%	15%
Contribution from air mass factors uncertainties	75%	30%
<ul style="list-style-type: none"> • from a priori profile errors • from model errors • from albedo errors • from cloud top pressure errors • from cloud fraction errors 	<ul style="list-style-type: none"> • 60% • 35% • 20% • 20% • 15% 	<ul style="list-style-type: none"> • 20% • 15% • 10% • 10% • 05%
Contribution from background correction uncertainties	40%	10%
Total	90%	35%
Total without smoothing error	50%	25%

702

703 **4. Verification**

704 In the framework of the TROPOMI L2 WG and QA4ECV projects, extensive comparisons of the prototype
 705 (this paper), the verification (IUP-UB), and alternative scientific algorithms (MPIC, KNMI, WUR) have been
 706 conducted. All follow a common DOAS approach. Prototype and verification algorithms have been applied to
 707 both synthetic and OMI spectra. Here, we present a selection of OMI results. For a complete description of the
 708 verification algorithm as well as results and discussion of the retrievals applied to synthetic spectra, please refer
 709 to the TROPOMI verification report (Richter et al., 2015).

710 **4.1 Harmonized DOAS fit settings using OMI test data**

711 For this exercise, a common set of DOAS fit parameters has been agreed upon. The goal of the intercomparison
 712 of harmonized fit settings was to ensure that the software implementation of the different algorithms behaves
 713 as expected in a large range of realistic measurement scenarios. Another objective was to gain knowledge on
 714 the level of agreement/disagreement of results from different groups when using the same settings, as well as
 715 on the main drivers for differences. Common and simple fit parameters based on the operational and
 716 verification algorithm were selected. They are summarized in Table 11.

717 **Table 11: Common DOAS fit settings for HCHO using OMI data.**

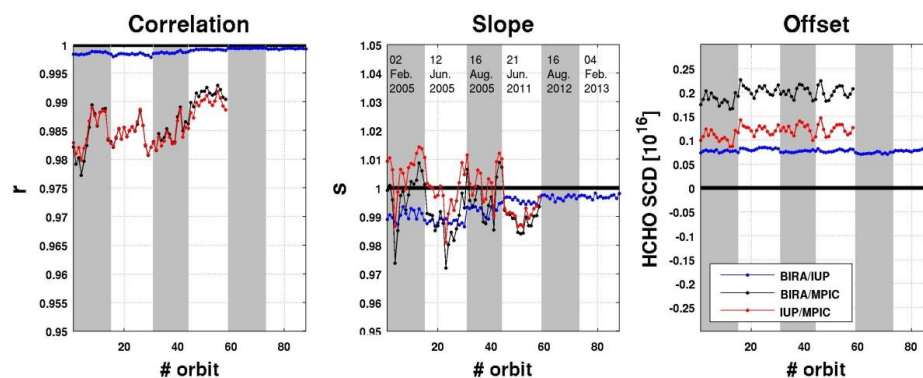
Parameter	Values
Fitting interval-1	328.5-359 nm
Calibration	1 interval (328-359 nm), using the SAO 2010 solar atlas (Chance and Kurucz, 2010).
Molecular species	HCHO, NO ₂ , Ozone, BrO, O ₂ -O ₂ : same cross-sections as in Table 4
Ring effect	Ring cross-section based on the technique outlined by Chance et al. (1997)
Slit function	One slit function per binned spectrum as a function of wavelength (60 OMI ISRF, Dirksen et al., 2006).
Polynomial	5 th order
Intensity offset correction	Linear offset (1/I ₀)
Reference spectrum I₀	Daily solar irradiance

718

719 The intercomparison of results using common settings allowed to identify and fix several issues in the different
 720 codes leading to an overall consolidation of the algorithms. It has been found that minor changes in the fit
 721 settings may lead to large offsets ($\pm 10 \times 10^{15}$ molec.cm⁻²) in the HCHO SCDs. However, an excellent level of
 722 agreement ($\pm 2 \times 10^{15}$ molec.cm⁻²) between the different retrieval codes was obtained after several iterations of
 723 the common settings. The main sources of discrepancies were found to be related to (1) the solar I₀ correction
 724 applied on the O₃ cross-sections, (2) the intensity offset correction, (3) the details of the wavelength calibration
 725 of the radiance and irradiance spectra, and (4) the OMI slit functions and their implementation in the
 726 convolution tools (Boersma et al., 2015).



727 An overview of the final SCD comparison is shown on Figure 12 for six test days at the beginning and the end
728 of the OMI time series, and for a particular OMI orbit on the left panel of Figure 13. The correlation coefficient,
729 slope and offset of linear regression fits performed on each comparison orbit are displayed. The correlation of
730 slant columns from BIRA and IUP-UB is extremely high in most cases. It is > 0.998 for all orbits. The slope
731 of the regression line between BIRA and IUP-UB results is close to 1.0. There is a constant offset of less than
732 1×10^{15} molec.cm⁻². The comparison between MPIC results and the two other algorithms gives somehow lower
733 correlations, but still larger than 0.98 from the beginning to the end of the OMI lifetime. Final deviations on
734 OMI HCHO SCD when using common settings were found to be of maximum $\pm 2\%$ (slope) and 2.5×10^{15}
735 molec.cm⁻². When relating the remaining differences in retrieved SCDs using common settings to the slant
736 column errors from the DOAS fit ($\sigma_{N,s,rand}$), it can be concluded that the differences between the results are
737 significantly smaller than the uncertainties (from 10 to 20% of $\sigma_{N,s,rand}$). Moreover, remaining offsets in SCDs
738 are further reduced by the background correction procedure.
739



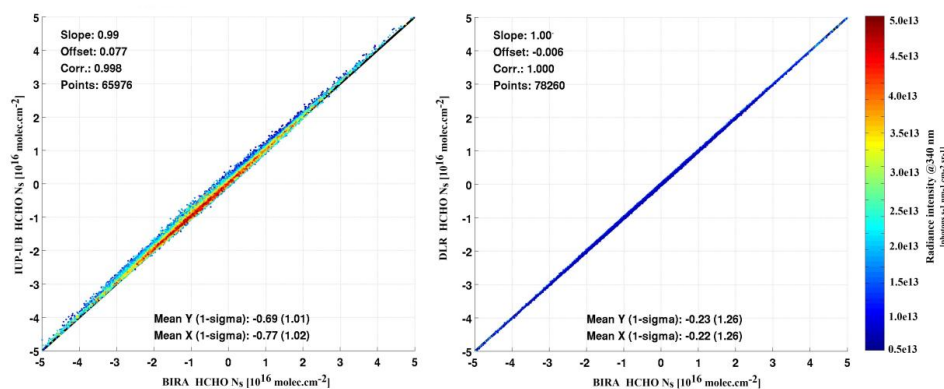
740

741 **Figure 12: Correlation (left), slope (middle) and offset (right) from a linear regression performed for**
742 **the common fit settings (see Table 11) for each orbit of OMI test days. A correlation plot for an**
743 **example orbit is provided in the left panel of Figure 13**Error! Reference source not found..

744 4.2 Verification of the operational implementation

745 A similar intercomparison exercise was performed with the operational algorithm UPAS, developed at DLR,
746 but using the exact settings of the prototype algorithm as detailed in Table 2. An example of resulting
747 correlation fit is shown in the right panel of Figure 13 for the same OMI orbit as for the comparison with the
748 IUP-UB results. The level of agreement between the prototype and operational results is found to be almost
749 perfect (correlation coefficient of 1, slope of 1.003 and offset of less than 0.2×10^{15} molec.cm⁻²), and very
750 satisfactory considering the sensitivity on small implementation changes.

751



752

753 **Figure 13: Correlation plots of HCHO slant columns retrieved with the BIRA prototype algorithm and**
754 **(left) the IUP-UB verification algorithm, (right) the operational processor, for OMI orbit number 2339**
755 **on 02/02/2005, including all pixels with SZA<80°.**

756

757 5. Validation

758 Independent validation activities are proposed and planned by the S5P Validation Team (Fehr, 2016) and within
759 the ESA S5P Mission Performance Center (MPC). The backbone of the formaldehyde validation is the MAX-
760 DOAS and FTIR networks operated as part of the Network for the Detection of Atmospheric Composition
761 Change (NDACC, www.ndsc.ncep.noaa.gov/) complemented by PANDONIA (pandonia.net/) and national
762 activities. In addition, model datasets will be used for validation as well as independent satellite retrievals.
763 Finally, airborne campaigns are planned to support the formaldehyde and other trace gases validation.

764 5.1 Requirements for validation

765 To validate the TROPOMI formaldehyde data products, comparisons with independent sources of HCHO
766 measurements are required. This includes comparisons with ground-based measurements, aircraft observations
767 and satellite data sets from independent sensors and algorithms. Moreover, not only information on the total
768 (tropospheric) HCHO column is needed but also information on its vertical distribution, especially in the lowest
769 three kilometres where the bulk of formaldehyde generally resides. In this altitude range, the a-priori vertical
770 profile shapes have the largest systematic impact on the satellite column errors. HCHO and aerosol profile
771 measurements are therefore needed.

772 The diversity of the NMVOC species, lifetimes and sources (biogenic, biomass burning or anthropogenic) calls
773 for validation data in a large range of locations worldwide (tropical, temperate and boreal forests, urban and
774 sub-urban areas). Continuous measurements are needed to obtain good statistics (as well for ground-based
775 measurements as for satellite columns) and to capture the seasonal variations. Validation and assessment of
776 consistency with historical satellite datasets require additional information on the HCHO diurnal variation,
777 which depends on the precursor emissions and on the local chemical regime.



778 The main emphasis is on quality assessment of retrieved HCHO column amounts on a global scale and over
 779 long time periods. The validation exercise will establish whether HCHO data quality meets the requirements
 780 of geophysical research applications like long term trend monitoring on the global scale, NMVOC source
 781 inversion, and research on the budget of tropospheric ozone. In addition, the validation will investigate the
 782 consistency between TROPOMI HCHO data and HCHO data records from other satellites.

783 5.2 Reference measurement techniques

784 Table 12 summarizes the type of data and measurements that can be used for the validation of the TROPOMI
 785 HCHO columns. The advantages and limitations of each technique are discussed. It should be noted that, unlike
 786 tropospheric O₃ or NO₂, the stratospheric contribution to the total HCHO column can be largely neglected
 787 which simplifies the interpretation of both satellite and ground-based measurements.

788 **Table 12: Data/Masurement types used for the validation of satellite HCHO columns. The**
 789 **information content of each type of measurement is qualitatively represented by the number of crosses.**

Type of measurement	Sensitivity in the boundary layer	Vertical profile information	Diurnal variation	Seasonal Variation	Total column	Earth coverage
MAX-DOAS	xxx	xx (3)	xxx	xxx	xx	xx
FTIR	x	-	xxx	xx	xxx	x
Direct Sun	xxx	-	xxx	xxx	xxx	x
In situ (1)	xx	-	xxx	xxx	-	xx
Aircraft (2)	xx	xxx	x	-	xx (4)	x
Satellite instruments	x	-	x	xxx	xx	xxx (5)

790

791 (1) Surface measurements that could be combined with regional modelling.

792 (2) Including ultra-light and unmanned airborne vehicles.

793 (3) Up to 2-3 km.

794 (4) Profiles generally need to be extrapolated.

795 (5) Different daily coverage and spatial resolutions.

796 The Multi-axis DOAS (MAX-DOAS) measurement technique has been developed to retrieve stratospheric and
 797 tropospheric trace gas total columns and profiles. The most recent generation of MAX-DOAS instruments
 798 allows for measurement of aerosols and a number of tropospheric pollutants, such as NO₂, HCHO, SO₂, O₄
 799 and CHOCHO (e.g. Irie et al., 2011). With the development of operational networks such as Pandonia
 800 (<http://pandonia.net/>), it is anticipated that many more MAX-DOAS instruments will become available in the
 801 near future to extend validation activities in other areas where HCHO emissions are significant. The locations
 802 where HCHO measurements are required are reviewed in the next section. Previous comparisons between
 803 GOME-2 and OMI HCHO monthly averaged columns with MAX-DOAS measurements recorded by BIRA-
 804 IASB in the Beijing city centre and in the sub-urban site of Xianghe showed that the systematic differences
 805 between the satellite and ground-based HCHO columns (about 20 to 40%) are almost completely explained



806 when taking into account the vertical averaging kernels of the satellite observations (De Smedt et al., 2015,
807 Wang et al., 2017), showing the importance of validating the a priori profiles as well.

808 HCHO columns can also be retrieved from the ground using FTIR spectrometers. In contrast to MAXDOAS
809 systems which essentially probe the first two kilometres of the atmosphere, FTIR instruments display a strong
810 sensitivity higher up in the free troposphere and are thus complementary to MAXDOAS (Vigouroux et al.,
811 2009). The deployment of FTIR instruments of relevance for HCHO is mostly taking place within the NDACC
812 network. Within the project NIDFORVal (S5P Nitrogen Dioxide and Formaldehyde Validation using NDACC
813 and complementary FTIR and UVVis networks), the number of FTIR stations providing HCHO time-series
814 has been raised from only 4 (Vigouroux et al., 2009; Jones et al., 2009; Viatte et al., 2014; Franco et al., 2015)
815 to 21. These stations are covering a wide range of HCHO concentrations, from clean Arctic or oceanic sites to
816 sub-urban and urban polluted sites, as well as sites with large biogenic emissions such as Porto Velho (Brazil)
817 or Wollongong (Australia).

818 Although ground-based remote-sensing DOAS and FTIR instruments are naturally best suited for the validation
819 of column measurements from space, in-situ instruments can also bring useful information. This type of
820 instrument can only validate surface HCHO concentrations, and therefore additional information on the vertical
821 profile (e.g. from regional modelling) is required to make the link with the satellite retrieved column. However,
822 in-situ instruments (where available) have the advantage to be continuously operated for pollution monitoring
823 in populated areas, allowing for extended and long term comparisons with satellite data (see e.g. Dufour et al.,
824 2009). Although more expensive and with a limited time and space coverage, aircraft campaigns provide
825 unique information on the HCHO vertical distributions (Zhu et al., 2017).

826 **5.3 Deployment of validation sites**

827 Sites operating correlative measurement should preferably be deployed at locations where significant NMVOC
828 sources exist. This includes:

- 829 • Tropical forests (Amazonian forest, Africa, Indonesia): The largest HCHO columns worldwide are
830 observed over these remote areas that are difficult to access. Biogenic and biomass burning emissions are
831 mixed. A complete year is needed to discriminate the various effects on the HCHO retrieval. Clouds tend
832 to have more systematic effects in tropical regions. Aircraft measurements are needed over biomass
833 burning areas.
- 834 • Temperate forests (South-Eastern US, China, Eastern Europe): In summer time, HCHO columns are
835 dominated by biogenic emissions. Those locations are useful to validate particular a-priori assumptions
836 such as model isoprene chemistry and OH oxidation scheme. Measurements are mostly needed from April
837 to September.
- 838 • Urban and sub-urban areas (Asian cities, California, European cities): Anthropogenic NMVOCs are more
839 diverse, and have a weaker contribution to the total HCHO column than biogenic NMVOCs. This type of
840 signal is therefore more difficult to validate. Continuous observations at mid-latitudes over a full year are
841 needed, to improve statistics.



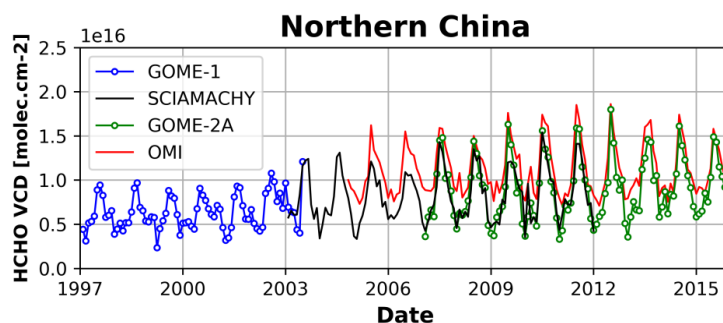
842 For adequate validation, the long-term monitoring should be complemented by dedicated campaigns. Ideally
843 such campaigns should be organised in appropriate locations such as e.g. South-Eastern US, Alabama where
844 biogenic NMVOCs and biogenic aerosols are emitted in large quantities during summer time, and should
845 include both aircraft and ground-based components.

846 5.4 Satellite-satellite intercomparisons

847 Satellite-satellite intercomparisons of HCHO columns are generally more straightforward than validation using
848 ground-based correlative measurements. Such comparisons are evaluated in a meaningful statistical sense
849 focusing on global patterns and regional averages, seasonality, scatter of values and consistency between
850 results and reported uncertainties. When intercomparing satellite measurements, special care has to be drawn
851 to:

- 852 • differences in spatial resolutions, resulting in possible offsets between satellite observations (van
853 der A et al., 2008; De Smedt et al., 2010; Hilboll et al., 2013),
- 854 • differences in overpass times, that holds valuable geophysical information about diurnal cycles
855 in emissions and chemistry (De Smedt et al., 2015; Stavrakou et al., 2015)
- 856 • differences in a priori assumptions.
- 857 • differences in the cloud algorithms and cloud correction schemes.

858 Assessing the consistency between successive satellite sensors is essential to allow for scientific studies making
859 use of the combination of several sensors. For example trends in NMVOC emissions have been successfully
860 derived from GOME(-2), SCIAMACHY, and OMI measurements (Figure 14). It is anticipated that TROPOMI,
861 the next GOME-2 instruments and the future Sentinel-4 and -5, will allow to extend these time series.



862

863 **Figure 14: HCHO columns over Northern China as observed with GOME (in blue), SCIAMACHY (in**
864 **black), GOME-2 (in green), and OMI (in red) (De Smedt et al., 2008; 2010; 2015).**



865 **6. Conclusions**

866 The retrieval algorithm for the TROPOMI formaldehyde product generation is based on the heritage from
867 algorithms successfully developed for the GOME, SCIAMACHY, GOME-2 and OMI sensors. A double-
868 interval fitting approach is implemented, following an algorithm baseline demonstrated on the GOME-2 and
869 OMI sensors. The HCHO retrieval algorithm also includes a post-processing across-track reference sector
870 correction to minimize OMI-type striping effects, if any. Additional features for future processor updates
871 include the use of daily earthshine radiance as reference selected in the remote Pacific spectral, outlier
872 screening during the fitting procedure (spike removal algorithm), and a more accurate background correction
873 scheme.

874 A detailed uncertainty budget is provided for every satellite observation. The precision of the HCHO
875 tropospheric column is expected to come close to the COPERNICUS product requirements in regions of high
876 emissions and, at mid-latitude, for summer (high sun) conditions. The trueness of the vertical columns is also
877 expected to be improved, owing to the use of daily forecasts for the estimation of HCHO vertical profile shapes,
878 that will be provided by a new version of the TM5-MP model, running at the spatial resolution of 1x1 degree
879 in latitude and longitude.

880 The validation of satellite retrievals in the lower troposphere is known to be challenging. Ground-based
881 measurements, where available, often sample the atmosphere at different spatial and temporal scales than the
882 satellite measurements, which leads to ambiguous comparisons. Additional correlative measurements are
883 needed over a variety of regions, in particular in the Tropics and at the sub-urban level in mid-latitudes. These
884 aspects are covered by a number of projects developed in the framework of the TROPOMI validation plan
885 (Fehr, 2016).

886

887 **Acknowledgements**

888 The TROPOMI HCHO algorithmic developments have been supported by the ESA Sentinel-5 Precursor Level-
889 2 Development project, as well as by the Belgian PRODEX (TRACE-S5P project). Multi-sensor HCHO
890 developments have been funded by the EU FP7 QA4ECV project (grant no. 607405), in close cooperation with
891 KNMI, University of Bremen, MPIC-Mainz and WUR.

892 **7. References**

- 893 Abbot, D. S., Palmer, P. I., Martin, R. V., Chance, K. V., Jacob, D. J. and Guenther, A.: Seasonal and
894 interannual variability of North American isoprene emissions as determined by formaldehyde column
895 measurements from space, *Geophys. Res. Lett.*, 30(17), 1886, 2003.
- 896 Barkley, M. P., Palmer, P. I., Ganzeveld, L., Arneth, A., Hagberg, D., Karl, T., Guenther, A., Paulot, F.,
897 Wennberg, P. O., Mao, J., Kurosu, T. P., et al.: Can a state of the art chemistry transport model simulate
898 Amazonian tropospheric chemistry?, *J. Geophys. Res.*, 116(D16), D16302, doi:10.1029/2011JD015893, 2011.
- 899 Barkley, M. P., Kurosu, T. P., Chance, K., Smedt, I. De, Van Roozendaal, M., Arneth, A., Hagberg, D.,
900 Guenther, A. and De Smedt, I.: Assessing sources of uncertainty in formaldehyde air mass factors over tropical
901 South America: Implications for top-down isoprene emission estimates, *J. Geophys. Res.*, 117(D13), D13304,
902 doi:10.1029/2011JD016827, 2012.
- 903 Barkley, M. P., De Smedt, I., Van Roozendaal, M., Kurosu, T. P., Chance, K. V., Arneth, A., Hagberg, D.,
904 Guenther, A. B., Paulot, F., Marais, E. A., others, et al.: Top-down isoprene emissions over tropical South
905 America inferred from SCIAMACHY and OMI formaldehyde columns, *J. Geophys. Res. Atmos.*, 118(12),
906 n/a–n/a, doi:10.1002/jgrd.50552, 2013.
- 907 Boersma, K. F., Eskes, H. J. and Brinksma, E. J.: Error analysis for tropospheric NO₂ retrieval from space, *J.*
908 *Geophys. Res.*, 109(D4), doi:10.1029/2003JD003962, 2004.
- 909 Boersma, K.F., Lorente, A., Muller, J. and the QA4ECV consortium: Recommendations (scientific) on best
910 practices for retrievals for Land and Atmosphere ECVs, QA4ECV D4.2, v0.8,
911 <http://www.qa4ecv.eu/sites/default/files/D4.2.pdf>, 2015.
- 912 Boersma, K. F., Vinken, G. C. M., and Eskes, H. J.: Representativeness errors in comparing chemistry transport
913 and chemistry climate models with satellite UV–Vis tropospheric column retrievals, *Geosci. Model Dev.*, 9,
914 875–898, <https://doi.org/10.5194/gmd-9-875-2016>, 2016.
- 915 Bovensmann, H., Peuch, V.-H., van Weele, M., Erbertseder, T., and Veihelmann, B.: Report Of The Review
916 Of User Requirements For Sentinels-4/-5, ESA, EO-SMA-/1507/JL, issue: 2.1, 2011.
- 917 Brion, J., et al.: Absorption spectra measurements for the ozone molecule in the 350–830 nm region, *J. Atmos.*
918 *Chem.*, 30, 291–299, 1998.
- 919 Castellanos, P., Boersma, K. F., Torres, O., and de Haan, J. F.: OMI tropospheric NO₂ air mass factors over
920 South America: effects of biomass burning aerosols, *Atmos. Meas. Tech.*, 8, 3831–3849, doi:10.5194/amt-8-
921 3831-2015, 2015.



- 922 Chance, K. and R. J. Spurr: Ring effect studies: Rayleigh scattering including molecular parameters for
923 rotational Raman scattering, and the Fraunhofer spectrum, *Applied Optics*, 36, 5224-5230, 1997.
- 924 Chance, K. V., Palmer, P. I., Martin, R. V., Spurr, R. J. D., Kurosu, T. P. and Jacob, D. J.: Satellite observations
925 of formaldehyde over North America from GOME, *Geophysical Research Letters*, 27(21), 3461-3464,
926 doi:10.1029/2000GL011857, 2000.
- 927 Chance, K. and Kurucz, R. L.: An improved high-resolution solar reference spectrum for earth's atmosphere
928 measurements in the ultraviolet, visible, and near infrared, *J. Quant. Spectrosc. Radiat. Transf.*, 111(9), 1289-
929 1295, 2010.
- 930 Chimot, J., Vlemmix, T., Veeffkind, J. P., de Haan, J. F. and Levelt, P. F.: Impact of aerosols on the OMI
931 tropospheric NO₂ retrievals over industrialized regions: how accurate is the aerosol correction of cloud-free
932 scenes via a simple cloud model?, *Atmos. Meas. Tech. Discuss.*, 8(8), 8385–8437, doi:10.5194/amt-d-8-8385-
933 2015, 2015.
- 934 Clémer, K., Van Roozendael, M., Fayt, C., Hendrick, F., Hermans, C., Pinardi, G., Spurr, R., Wang, P., and
935 De Mazière, M.: Multiple wavelength retrieval of tropospheric aerosol optical properties from MAXDOAS
936 measurements in Beijing, *Atmos. Meas. Tech.*, 3, 863-878, 2010.
- 937 Curci, G., Palmer, P. I., Kurosu, T. P., Chance, K. and Visconti, G.: Estimating European volatile organic
938 compound emissions using satellite observations of formaldehyde from the Ozone Monitoring Instrument,
939 *Atmos. Chem. Phys.*, 10(23), 11501-11517, 2010.
- 940 Danckaert, T., Fayt, C., Van Roozendael, M., De Smedt, I., Letocart, V., Merlaud, A., Pinardi, G: Qdoas
941 Software User Manual, Version 2.1, [http://uv-
942 vis.aeronomie.be/software/QDOAS/QDOAS_manual_2.1_201212.pdf](http://uv-vis.aeronomie.be/software/QDOAS/QDOAS_manual_2.1_201212.pdf), 2012.
- 943 Danielson, J.J., and Gesch, D.B.: Global multi-resolution terrain elevation data 2010 (GMTED2010): U.S.
944 Geological Survey Open-File Report 2011–1073, 26 p, 2011.
- 945 Daumont, M., Brion, J., Charbonnier, J., and Malicet, J.: Ozone UV spectroscopy, I: Absorption cross-sections
946 at room temperature, *J. Atmos. Chem.*, 15, 145–155, 1992.
- 947 De Smedt, I., Müller, J.-F., Stavrou, T., van der A, R., Eskes, H. and Van Roozendael, M.: Twelve years of
948 global observations of formaldehyde in the troposphere using GOME and SCIAMACHY sensors, *Atmos.
949 Chem. Phys.*, 8(16), 4947-4963, 2008.
- 950 De Smedt, I., Stavrou, T., Müller, J. F., van Der A, R. J. and Van Roozendael, M.: Trend detection in satellite
951 observations of formaldehyde tropospheric columns, *Geophys. Res. Lett.*, 37(18), L18808,
952 doi:10.1029/2010GL044245, 2010.



- 953 De Smedt, I.: Long-Term Global Observations of Tropospheric Formaldehyde Retrieved from Spaceborne
954 Nadir UV Sensors, Ph.D. thesis, Universite Libre De Bruxelles, Laboratoire do Chimie Quantique et
955 Photophysique, Faculté de Sciences Appliquées, 2011.
- 956 De Smedt, I., Van Roozendael, M., Stavroukou, T., Müller, J.-F., Lerot, C., Theys, N., Valks, P., Hao, N., and
957 van der A, R.: Improved retrieval of global tropospheric formaldehyde columns from GOME-2/MetOp-A
958 addressing noise reduction and instrumental degradation issues, *Atmos. Meas. Tech. Discuss.*, 5, 5571-5616,
959 doi:10.5194/amt-5-5571-2012, Special Issue: GOME-2: calibration, algorithms, data products and validation,
960 2012.
- 961 De Smedt, I., Stavroukou, T., Hendrick, F., Danckaert, T., Vlemmix, T., Pinardi, G., Theys, N., Lerot, C., Gielen,
962 C., Vigouroux, C., Hermans, C., et al.: Diurnal, seasonal and long-term variations of global formaldehyde
963 columns inferred from combined OMI and GOME-2 observations, *Atmos. Chem. Phys. Discuss.*, 15(8),
964 12241–12300, doi:10.5194/acpd-15-12241-2015, 2015.
- 965 Dirksen, R., Dobber, M., Voors, R., and Levelt, P.: Prelaunch characterization of the Ozone Monitoring
966 Instrument transfer function in the spectral domain, *Appl. Opt.*, 45(17), 3972-3981, 2006.
- 967 Dufour, G., F. Wittrock, M. Camredon, M. Beekmann, A. Richter, B. Aumont, and J. P. Burrows,
968 SCIAMACHY formaldehyde observations: constraint for isoprene emission estimates over Europe?, *Atmos.*
969 *Chem. Phys.*, 9(5), 1647-1664, 2009.
- 970 Eskes, H. J. and K. F. Boersma, Averaging kernels for DOAS total-column satellite retrievals, *Atmos. Chem.*
971 *Phys.*, 3, 1285-1291, 2003.
- 972 Fayt, C. and M. Van Roozendael: Windoas 2.1, Software User Manual, BIRA-IASB, 2001.
- 973 Fehr, T.: Sentinel-5 Precursor Scientific Validation Implementation Plan, EOP-SM/2993/TF-tf, 1.0,
974 <http://doi.org/10.5281/zenodo.165739>, 2016.
- 975 Fleischmann, O. C., et al.: New ultraviolet absorption cross-sections of BrO at atmospheric temperatures
976 measured by time-windowing Fourier transform spectroscopy, *J. Photochem. Photobiol. A*, 168, 117–132,
977 2004.
- 978 Fortems-Cheiney, A., Chevallier, F., Pison, I., Bousquet, P., Saunio, M., Szopa, S., Cressot, C., Kurosu, T. P.,
979 Chance, K. and Fried, A.: The formaldehyde budget as seen by a global-scale multi-constraint and multi-
980 species inversion system, *Atmos. Chem. Phys. Discuss.*, 12(3), 6909-6955, doi:10.5194/acpd-12-6909-2012,
981 2012.
- 982 Franco, B., Hendrick, F., Van Roozendael, M., Müller, J.-F., Stavroukou, T., Marais, E. A., Bovy, B., Bader,
983 W., Fayt, C., Hermans, C., Lejeune, B., Pinardi, G., Servais, C., and Mahieu, E.: Retrievals of formaldehyde
984 from ground-based FTIR and MAX-DOAS observations at the Jungfraujoch station and comparisons with



- 985 GEOS-Chem and IMAGES model simulations, *Atmos. Meas. Tech.*, 8, 1733-1756,
986 <https://doi.org/10.5194/amt-8-1733-2015>, 2015.
- 987 Fu, T.-M., Jacob, D. J., Palmer, P. I., Chance, K. V., Wang, Y. X., Barletta, B., Blake, D. R., Stanton, J. C. and
988 Pilling, M. J.: Space-based formaldehyde measurements as constraints on volatile organic compound emissions
989 in east and south Asia and implications for ozone, *J. Geophys. Res.*, 112(D6), D06312, 2007.
- 990 González Abad, G., Liu, X., Chance, K., Wang, H., Kurosu, T. P. and Suleiman, R.: Updated Smithsonian
991 Astrophysical Observatory Ozone Monitoring Instrument (SAO OMI) formaldehyde retrieval, *Atmos. Meas.*
992 *Tech.*, 8(1), 19–32, doi:10.5194/amt-8-19-2015, 2015.
- 993 Gonzi, S., Palmer, P. I., Barkley, M. P., De Smedt, I. and Van Roozendael, M.: Biomass burning emission
994 estimates inferred from satellite column measurements of HCHO: Sensitivity to co-emitted aerosol and
995 injection height, *Geophys. Res. Lett.*, 38(14), L14807, doi:10.1029/2011GL047890, 2011.
- 996 Gottwald, M., Bovensmann, H. et al.: *SCIAMACHY, Monitoring the Changing Earth's Atmosphere*, DLR,
997 Institut für Methodik der Fernerkundung (IMF), 2006.
- 998 Grainger, J. F. and J. Ring: Anomalous Fraunhofer line profiles, *Nature*, 193, 762, 1962.
- 999 Greenblatt, G. D., Orlando, J. J., Burkholder, J. B., and Ravishankara, A. R.: Absorption measurements of
1000 oxygen between 330 and 1140 nm, *J. Geophys. Res.*, 95(D11), 18 577–18 582, doi:10.1029/90JD01375, 1990.
- 1001 Hassinen, S., Balis, D., Bauer, H., Begoin, M., Delcloo, A., Eleftheratos, K., Gimeno Garcia, S., Granville, J.,
1002 Grossi, M., Hao, N., Hedelt, P., Hendrick, F., Hess, M., Heue, K.-P., Hovila, J., Jönch-Sørensen, H., Kalakoski,
1003 N., Kauppi, A., Kiemle, S., Kins, L., Koukouli, M. E., Kujanpää, J., Lambert, J.-C., Lang, R., Lerot, C., Loyola,
1004 D., Pedergnana, M., Pinardi, G., Romahn, F., Van Roozendael, M., Lutz, R., De Smedt, I., Stammes, P.,
1005 Steinbrecht, W., Tamminen, J., Theys, N., Tilstra, L. G., Tuinder, O. N. E., Valks, P., Zerefos, C., Zimmer, W.
1006 and Zyrrichidou, I.: Overview of the O3M SAF GOME-2 operational atmospheric composition and UV
1007 radiation data products and data availability, *Atmos. Meas. Tech.*, 9(2), 383–407, doi:10.5194/amt-9-383-2016,
1008 2016.
- 1009 Heckel, A., Kim, S.-W., Frost, G. J., Richter, A., Trainer, M. and Burrows, J. P.: Influence of low spatial
1010 resolution a priori data on tropospheric NO₂ satellite retrievals, *Atmos. Meas. Tech.*, 4(9), 1805–1820,
1011 doi:10.5194/amt-4-1805-2011, 2011.
- 1012 Hewson, W., Bösch, H., Barkley, M. P. and De Smedt, I.: Characterisation of GOME-2 formaldehyde retrieval
1013 sensitivity, *Atmospheric Measurement Techniques*, 6(2), 371–386, doi:10.5194/amt-6-371-2013, 2013.
- 1014 Hilboll, A., Richter, A. and Burrows, J. P.: Long-term changes of tropospheric NO₂ over megacities derived
1015 from multiple satellite instruments, *Atmospheric Chemistry and Physics*, 13(8), 4145–4169, doi:10.5194/acp-
1016 13-4145-2013, 2013.



- 1017 Huijnen, V., Williams, J., van Weele, M., van Noije, T., Krol, M., Dentener, F., Segers, A., Houweling, S.,
1018 Peters, W., de Laat, J., Boersma, F., Bergamaschi, P., van Velthoven, P., Le Sager, P., Eskes, H., Alkemade,
1019 F., Scheele, R., Nédélec, P., and Pätz, H.-W., The global chemistry transport model tm5: description and
1020 evaluation of the tropospheric chemistry version 3.0., *Geoscientific Model Development*, 3(2):445-473, 2010.
- 1021 Jones, N. B., Riedel, K., Allan, W., Wood, S., Palmer, P. I., Chance, K., and Notholt, J.: Long-term tropospheric
1022 formaldehyde concentrations deduced from ground-based fourier transform solar infrared measurements,
1023 *Atmos. Chem. Phys.*, 9, 7131-7142, <https://doi.org/10.5194/acp-9-7131-2009>, 2009.
- 1024 Kleipool, Q. L., Dobber, M. R., de Haan, J. F. and Levelt, P. F.: Earth surface reflectance climatology from 3
1025 years of OMI data, *J. Geophys. Res.*, 113(D18), D18308, doi:10.1029/2008JD010290, 2008.
- 1026 Koelemeijer, R. B. A., Stammes, P., Hovenier, J. W. and de Haan, J. F.: A fast method for retrieval of cloud
1027 parameters using oxygen A band measurements from the Global Ozone Monitoring Experiment, *J. Geophys.*
1028 *Res.*, 106(D4), 3475-3490, doi:10.1029/2000JD900657, 2001.
- 1029 Khokhar, M. F.: Spatio-Temporal Analyses of Formaldehyde over Pakistan by Using SCIAMACHY and
1030 GOME-2 Observations, *Aerosol Air Qual. Res.*, 1–14, doi:10.4209/aaqr.2014.12.0339, 2015.
- 1031 Krol, M., Houweling, S., Bregman, B., van den Broek, M., Segers, A., van Velthoven, P., Peters, W., Dentener,
1032 F., and Bergamaschi, P.: The two-way nested global chemistry-transport zoom model TM5: algorithm and
1033 applications., *Atmos. Chem. Phys.*, 5(2):417-432, 2005.
- 1034 Kurosu, T. P., OMHCHO README FILE,
1035 http://www.cfa.harvard.edu/tkurosu/SatelliteInstruments/OMI/PGEReleases/READMEs/OMHCHO_READ
1036 [ME.pdf](http://www.cfa.harvard.edu/tkurosu/SatelliteInstruments/OMI/PGEReleases/READMEs/OMHCHO_READ), last access: 14/08/2012, 2008.
- 1037 Langen, J., Meijer, Y., Brinksma, E., Veihelmann, B., and Ingmann, P.: GMES Sentinels 4 and 5 Mission
1038 Requirements Document (MRD), ESA, EO-SMA-/1507/JL, issue: 3, 2011.
- 1039 Langen, J., Meijer, Y., Brinksma, E., Veihelmann, B., and Ingmann, P.: Copernicus Sentinels 4 and 5 Mission
1040 Requirements Traceability Document (MRTD), ESA, EO-SMA-/1507/JL, issue: 2, 2017.
- 1041 Leitao, J., Richter, A., Vrekoussis, M., Kokhanovsky, A., Zhang, Q.J., Beekmann, M., and Burrows, J. P.: On
1042 the improvement of NO₂ satellite retrievals – aerosol impact on the airmass factors, *Atmos. Meas. Tech.*, 3,
1043 475–493, doi:10.5194/amt-3-475-2010,2010.
- 1044 Leue, C.: Detektion der troposphärischen NO₂ Daten anhand von GOME. Ph.D. thesis, Univ. Heidelberg,
1045 Heidelberg, Germany, 1999.



- 1046 Li, C., Joiner, J., Krotkov, N. A. and Dunlap, L.: A New Method for Global Retrievals of HCHO Total Columns
1047 from the Suomi National Polar-orbiting Partnership Ozone Monitoring and Profiler Suite, *Geophys. Res. Lett.*,
1048 doi:10.1002/2015GL063204, 2015.
- 1049 Lin, J. T., Martin, R. V., Boersma, K. F., Sneep, M., Stammes, P., Spurr, R., Wang, P., Van Roozendaal, M.,
1050 Clemer, K. and Irie, H.: Retrieving tropospheric nitrogen dioxide from the Ozone Monitoring Instrument:
1051 Effects of aerosols, surface reflectance anisotropy, and vertical profile of nitrogen dioxide, *Atmos. Chem.*
1052 *Phys.*, 14(3), 1441–1461, doi:10.5194/acp-14-1441-2014, 2014.
- 1053 Lorente, A., Boersma, K. F., Yu, H., Dörner, S., Hilboll, A., Richter, A., Liu, M., Lamsal, L. N., Barkley, M.,
1054 De Smedt, I., Van Roozendaal, M., Wang, Y., Wagner, T., Beirle, S., Lin, J. T., Krotkov, N., Stammes, P.,
1055 Wang, P., Eskes, H. J., and Krol, M.: Structural uncertainty in air mass factor calculation for NO₂ and HCHO
1056 satellite retrievals, *Atmos. Meas. Tech. Discuss.*, doi:10.5194/amt-2016-306, in review, 2016.
- 1057 Loyola, D. G., Gimeno García, S., Lutz, R., Romahn, F., Spurr, R. J. D., Pedernana, M., Doicu, A., and
1058 Schüssler, O.: The operational cloud retrieval algorithms from TROPOMI on board Sentinel-5 Precursor,
1059 *Atmos. Meas. Tech. Discuss.*, <https://doi.org/10.5194/amt-2017-128>, in review, 2017.
- 1060 Mahajan, A. S., De Smedt, I., Biswas, M. S., Ghude, S., Fadnavis, S., Roy, C. and van Roozendaal, M.: Inter-
1061 annual variations in satellite observations of nitrogen dioxide and formaldehyde over India, *Atmos. Environ.*,
1062 116, 194–201, doi:10.1016/j.atmosenv.2015.06.004, 2015.
- 1063 Malicet, C., Daumont, D., Charbonnier, J., Parisse, C., Chakir, A., and Brion, J.: Ozone UV spectroscopy, II:
1064 Absorption cross-sections and temperature dependence, *J. Atmos. Chem.*, 21, 263–273, 1995.
- 1065 Marais, E. A., Jacob, D. J., Kurosu, T. P., Chance, K., Murphy, J. G., Reeves, C., Mills, G., Casadio, S., Millet,
1066 D. B., Barkley, M. P., Paulot, F., et al.: Isoprene emissions in Africa inferred from OMI observations of
1067 formaldehyde columns, *Atmos. Chem. Phys. Discuss.*, 12(3), 7475–7520, doi:10.5194/acpd-12-7475-2012,
1068 2012.
- 1069 Marbach, T., Beirle, S., Platt, U., Hoor, P., Wittrock, F., Richter, A., Vrekoussis, M., Grzegorski, M., Burrows,
1070 J. P. and Wagner, T.: Satellite measurements of formaldehyde linked to shipping emissions, *Atmos. Chem.*
1071 *Phys.*, 9(21), 2009.
- 1072 Martin, R. V., Chance, K. V., Jacob, D. J., Kurosu, T. P., Spurr, R. J. D., Bucsele, E. J., Gleason, J., Palmer, P.
1073 I., Bey, I., Fiore, A. M., Li, Q., et al.: An improved retrieval of tropospheric nitrogen dioxide from GOME, *J.*
1074 *Geophys. Res.*, 107(D20), doi:10.1029/2001JD001027, 2002.
- 1075 Meller, R., and Moortgat, G. K.: Temperature dependence of the absorption cross section of HCHO between
1076 223 and 323K in the wavelength range 225–375 nm, *J. Geophys. Res.*, 105(D6), 7089–7102,
1077 doi:10.1029/1999JD901074, 2000.



- 1078 Millet, D. B., Jacob, D. J., Boersma, K. F., Fu, T.-M., Kurosu, T. P., Chance, K. V., Heald, C. L. and Guenther,
1079 A.: Spatial distribution of isoprene emissions from North America derived from formaldehyde column
1080 measurements by the OMI satellite sensor, *Journal of Geophysical Research*, 113(D2), 1-18,
1081 doi:10.1029/2007JD008950, 2008.
- 1082 Palmer, P. I., Jacob, D. J., Chance, K. V., Martin, R. V., D, R. J., Kurosu, T. P., Bey, I., Yantosca, R. and Fiore,
1083 A.: Air mass factor formulation for spectroscopic measurements from satellites: Application to formaldehyde
1084 retrievals from the Global Ozone Monitoring Experiment, *Journal of Geophysical Research*, 106(D13), 14539-
1085 14550, doi:10.1029/2000JD900772, 2001.
- 1086 Palmer, P. I., Abbot, D. S., Fu, T.-M., Jacob, D. J., Chance, K. V., Kurosu, T. P., Guenther, A., Wiedinmyer,
1087 C., Stanton, J. C., Pilling, M. J., Pressley, S. N., et al.: Quantifying the seasonal and interannual variability of
1088 North American isoprene emissions using satellite observations of the formaldehyde column, *Journal of*
1089 *Geophysical Research*, 111(D12), 1-14, doi:10.1029/2005JD006689, 2006.
- 1090 Pedernana, M., Loyola, D., Apituley, A., Sneep, M., Veefkind, J. P.: Sentinel-5 precursor/TROPOMI Level
1091 2 Product User Manual Formaldehyde HCHO, S5P-L2-DLR-PUM-400F, 0.11.4,
1092 [http://www.tropomi.eu/sites/default/files/files/S5P-L2-DLR-PUM-400F-](http://www.tropomi.eu/sites/default/files/files/S5P-L2-DLR-PUM-400F-Product_User_Manual_for_the_Sentinel_5_precursor_Formaldehyde_HCHO-00.11.04-20170601_signed.pdf)
1093 [Product_User_Manual_for_the_Sentinel_5_precursor_Formaldehyde_HCHO-00.11.04-](http://www.tropomi.eu/sites/default/files/files/S5P-L2-DLR-PUM-400F-Product_User_Manual_for_the_Sentinel_5_precursor_Formaldehyde_HCHO-00.11.04-20170601_signed.pdf)
1094 [20170601_signed.pdf](http://www.tropomi.eu/sites/default/files/files/S5P-L2-DLR-PUM-400F-Product_User_Manual_for_the_Sentinel_5_precursor_Formaldehyde_HCHO-00.11.04-20170601_signed.pdf), 2017.
- 1095 Pinardi, G., Van Roozendaal, M., Abuhassan, N., Adams, C., Cede, a., Clémer, K., Fayt, C., Frieß, U., Gil, M.,
1096 Herman, J., Hermans, C., et al.: MAX-DOAS formaldehyde slant column measurements during CINDI:
1097 intercomparison and analysis improvement, *Atmospheric Measurement Techniques*, 6(1), 167–185,
1098 doi:10.5194/amt-6-167-2013, 2013.
- 1099 Platt, U.: Differential optical absorption spectroscopy (DOAS), in *Air Monitoring by Spectroscopic*
1100 *Techniques*, M.W. Sigrist ed., Chemical Analysis Series, Wiley, New York, 127, 27-84, 1994.
- 1101 Platt, U and Stutz, J.: *Differential Optical Absorption Spectroscopy: Principles and Applications (Physics of*
1102 *Earth and Space Environments)*, Springer-Verlag, Berlin, Heidelberg, ISBN 978-3540211938, 2008.
- 1103 Puķīte, J., Kühl, S., Deutschmann, T., Platt, U., and Wagner, T.: Extending differential optical absorption
1104 spectroscopy for limb measurements in the UV, *Atmos. Meas. Tech.*, 3, 631-653, 2010.
- 1105 Richter, A., Begoin, M., Hilboll, A. and Burrows, J. P.: An improved NO₂ retrieval for the GOME-2 satellite
1106 instrument, *Atmos. Meas. Tech.*, 4(6), 213-246, doi:10.5194/amt-4-1147-2011, 2011.
- 1107 Richter, A. and S5-P verification teams: S5P/TROPOMI Science Verification Report, S5P-IUP-L2-ScVR-RP,
1108 v2.1, 2015-12-22, in *Level-2 Algorithm Developments for Sentinel-5 Precursor*, 2015.



- 1109 Rodgers, C. D.: Inverse Methods for Atmospheric Sounding, Theory and Practice, World Scientific Publishing,
1110 Singapore-New-Jersey-London-Hong Kong, 2000.
- 1111 Rodgers, C. D., and B. J. Connor: Intercomparison of remote sounding instruments, *J. Geophys. Res.*, 108,
1112 doi:10.1029/2002JD002299, 2003.
- 1113 Serdyuchenko, A., Gorshchev, V., Weber, M., Chehade, W., and Burrows, J. P.: High spectral resolution ozone
1114 absorption cross-sections – Part 2: Temperature dependence, *Atmos. Meas. Tech.*, 7, 625-636,
1115 doi:10.5194/amt-7-625-2014, 2014.
- 1116 Spurr, R. J. D.: LIDORT and VLIDORT: Linearized pseudo-spherical scalar and vector discrete ordinate
1117 radiative transfer models for use in remote sensing retrieval problems, in *Light Scattering Reviews*, edited by
1118 A. Kokhanovsky, pp. 229–271, Berlin, 2008a.
- 1119 Spurr, R. J. D., J. de Haan, R. van Oss, and A. Vasilkov, Discrete ordinate radiative transfer in a stratified
1120 medium with first-order rotational Raman scattering, *J.Q.S.R.T* 109, Iss. 3, 404425, 2008b.
- 1121 Stavrakou, T., Müller, J. F., De Smedt, I., Van Roozendael, M., van der Werf, G. R., Giglio, L. and Guenther,
1122 A.: Global emissions of non-methane hydrocarbons deduced from SCIAMACHY formaldehyde columns
1123 through 2003–2006, *Atmos. Chem. Phys.*, 9(3), 1037-1060, 2009a.
- 1124 Stavrakou, T., Smedt, I. D., Roozendael, M. V., Vrekoussis, M., Wittrock, F., Burrows, J., Building, M., Lane,
1125 B., Gifford, C. and Kingdom, U.: The continental source of glyoxal estimated by the synergistic use of
1126 spaceborne measurements and inverse modelling, 2009b.
- 1127 Stavrakou, T., Müller, J.-F., Bauwens, M., De Smedt, I., Van Roozendael, M., Guenther, a., Wild, M. and Xia,
1128 X.: Isoprene emissions over Asia 1979–2012: impact of climate and land-use changes, *Atmos. Chem. Phys.*,
1129 14(9), 4587–4605, doi:10.5194/acp-14-4587-2014, 2014.
- 1130 Stavrakou, T., Müller, J., Bauwens, M., Smedt, I. De and Roozendael, M. Van: How consistent are top-down
1131 hydrocarbon emissions based on formaldehyde observations from GOME-2 and OMI ?, *Atmos. Chem. Phys.*
1132 Discuss., 12007–12067, doi:10.5194/acpd-15-12007-2015, 2015.
- 1133 Stein Zweers et al., TROPOMI ATBD of the UV aerosol index, S5P-KNMI-L2-0008-RP, 1.0,
1134 [http://www.tropomi.eu/sites/default/files/files/S5P-KNMI-L2-0008-RP-TROPOMI_ATBD_UVAI-v1p0p0-](http://www.tropomi.eu/sites/default/files/files/S5P-KNMI-L2-0008-RP-TROPOMI_ATBD_UVAI-v1p0p0-20160203.pdf)
1135 [20160203.pdf](http://www.tropomi.eu/sites/default/files/files/S5P-KNMI-L2-0008-RP-TROPOMI_ATBD_UVAI-v1p0p0-20160203.pdf), 2016
- 1136 Tanskanen, A. Lambertian Surface Albedo Climatology at 360 nm from TOMS Data Using Moving Time-
1137 Window Technique. In: *Proceedings of the XX Quadrennial Ozone Symposium*, 1-8 June 2004, Kos, Greece.



- 1138 Thalman, R. and Volkamer, R.: Temperature dependent absorption cross-sections of O₂-O₂ collision pairs
1139 between 340 and 630 nm and at atmospherically relevant pressure., *Phys. Chem. Chem. Phys.*, 15(37), 15371–
1140 81, doi:10.1039/c3cp50968k, 2013.
- 1141 Theys, N., De Smedt, I., Yu, H., Danckaert, T., van Gent, J., Hörmann, C., Wagner, T., Hedelt, P., Bauer, H.,
1142 Romahn, F., Pedergnana, M., Loyola, D. and Van Roozendael, M.: Sulfur dioxide retrievals from TROPOMI
1143 onboard Sentinel-5 Precursor: algorithm theoretical basis, *Atmos. Meas. Tech.*, 10(January), 119–153,
1144 doi:10.5194/amt-10-119-2017, 2017.
- 1145 U.S. Standard Atmosphere, U.S. Government Printing Office, Washington, D.C., 1976.
- 1146 Vandaele A.C., C. Hermans, P.C. Simon, M. Carleer, R. Colin, S. Fally, M.F. Méridienne, A. Jenouvrier, and B.
1147 Coquart, Measurements of the NO₂ absorption cross-section from 42000 cm⁻¹ to 10000 cm⁻¹ (238-1000 nm)
1148 at 220 K and 294 K, *J.Q.S.R.T.*, 59, 171-184, 1998.
- 1149 van der A, R.J., H.J. Eskes, K.F. Boersma, T.P. van Noije, et al., Trends, seasonal variability and dominant
1150 NO_x source derived from a ten year record of NO₂ measured from space, *J. Geophys. Res.*, 113, D04302, doi:
1151 10.1029/2007JD009021, 2008.
- 1152 van Geffen, J.H.G.M., K.F. Boersma, H.J. Eskes, J.D. Maasackers and J.P. Veefkind, TROPOMI ATBD of
1153 the total and tropospheric NO₂ data products, S5P-KNMI-L2-0005-RP, 1.1.0,
1154 [http://www.tropomi.eu/sites/default/files/files/S5P-KNMI-L2-0005-RP-](http://www.tropomi.eu/sites/default/files/files/S5P-KNMI-L2-0005-RP-TROPOMI_ATBD_NO2_data_products-v1p1p0-20170816_signed.pdf)
1155 [TROPOMI_ATBD_NO2_data_products-v1p1p0-20170816_signed.pdf](http://www.tropomi.eu/sites/default/files/files/S5P-KNMI-L2-0005-RP-TROPOMI_ATBD_NO2_data_products-v1p1p0-20170816_signed.pdf), 2017.
- 1156 Van Roozendael, M., V. Soebijanta, C. Fayt, and J.-C. Lambert: Investigation of DOAS Issues Affecting the
1157 Accuracy of the GDP Version 3.0 Total Ozone Product, in *ERS-2 GOME GDP 3.0 Implementation and Delta*
1158 *Validation, ERSE-DTEX-EOAD-TN-02-0006, ESA/ESRIN, Frascati, Italy, Chap.6, pp.97-129, 2002.*
- 1159 Van Roozendael, M., Spurr, R., Loyola, D., Lerot, C., Balis, D., Lambert, J.-C., Zimmer, W., Van Gent, J.,
1160 Van Geffen, J., Koukouli, M., Granville, J., Doicu, A., Fayt, C. & Zehner, C.: Sixteen Years Of GOME/ERS-
1161 2 Total Ozone Data: The New Direct-Fitting Gome Data Processor (Gdp) Version 5 - Algorithm Description,
1162 *J.geophys. Res.*, 117, D03305, Doi: 10.1029/2011jd016471, 2012.
- 1163 van Weele, M., Levelt, P., Aben, I., Veefkind, P., Dobber, M., Eskes, H., Houweling, S., Landgraf, J.,
1164 Noordhoek, R.: Science Requirements Document for TROPOMI. Volume 1, KNMI & SRON, RS-
1165 TROPOMI-KNMI-017, issue: 2.0, 2008.
- 1166 Veefkind, J. P., Aben, I., McMullan, K., Förster, H., de Vries, J., Otter, G., Claas, J., Eskes, H. J., de Haan, J.
1167 F., Kleipool, Q., van Weele, M., et al.: TROPOMI on the ESA Sentinel-5 Precursor: A GMES mission for
1168 global observations of the atmospheric composition for climate, air quality and ozone layer applications,
1169 *Remote Sensing of Environment*, 120(0), 70-83, 2012.



- 1170 Veefkind, J. P., de Haan, J. F., Sneep, M., and Levelt, P. F.: Improvements to the OMI O₂-O₂ operational
1171 cloud algorithm and comparisons with ground-based radar-lidar observations, *Atmos. Meas. Tech.*, 9, 6035-
1172 6049, <https://doi.org/10.5194/amt-9-6035-2016>, 2016.
- 1173 Viatte, C., Strong, K., Walker, K. A., and Drummond, J. R.: Five years of CO, HCN, C₂H₆, C₂H₂, CH₃OH,
1174 HCOOH and H₂CO total columns measured in the Canadian high Arctic, *Atmos. Meas. Tech.*, 7, 1547-1570,
1175 <https://doi.org/10.5194/amt-7-1547-2014>, 2014.
- 1176 Vigouroux, C., F. Hendrick, T. Stavrakou, B. Dils, I. De Smedt, C. Hermans, A. Merlaud, F. Scolas, C. Senten,
1177 G. Vanhaelewyn, S. Fally, M. Carleer, J.-M. Metzger, J.-F. Müller, M. Van Roozendael, and M. De Mazière,
1178 Ground-based FTIR and MAX-DOAS observations of formaldehyde at Réunion Island and comparisons with
1179 satellite and model data, *Atmos. Chem. Phys.*, 9, 9523-9544, doi:10.5194/acp-9-9523-2009.
- 1180 Vountas, M., Rozanov, V. V. and Burrows, J. P.: Ring effect: impact of rotational Raman scattering on radiative
1181 transfer in earth's atmosphere, *J. of Quant. Spec. and Rad. Trans.*, 60(6), 943-961, 1998.
- 1182 Vrekoussis, M., Wittrock, F., Richter, A. and Burrows, J. P.: GOME-2 observations of oxygenated VOCs:
1183 what can we learn from the ratio glyoxal to formaldehyde on a global scale?, *Atmos. Chem. Phys.*, 10(21),
1184 10145-10160, 2010.
- 1185 Williams, J. E., Boersma, K. F., Le Sager, P., and Verstraeten, W. W.: The high-resolution version of TM5-
1186 MP for optimized satellite retrievals: description and validation, *Geosci. Model Dev.*, 10, 721-750,
1187 doi:10.5194/gmd-10-721-2017, 2017.
- 1188 Wittrock, F., Richter, A., Oetjen, H., Burrows, J. P., Kanakidou, M., Myriokefalitakis, S., Volkamer, R., Beirle,
1189 S., Platt, U. and Wagner, T.: Simultaneous global observations of glyoxal and formaldehyde from space,
1190 *Geophysical Research Letters*, 33(16), 1-5, doi:10.1029/2006GL026310, 2006.
- 1191 Zhu, L., Jacob, D. J., Kim, P. S., Fisher, J. A., Yu, K., Travis, K. R., Mickleby, L. J., Yantosca, R. M., Sulprizio,
1192 M. P., De Smedt, I., Gonzalez Abad, G., Chance, K., Li, C., Ferrare, R., Fried, A., Hair, J. W., Hanisco, T. F.,
1193 Richter, D., Scarino, A. J., Walega, J., Weibring, P. and Wolfe, G. M.: Observing atmospheric formaldehyde
1194 (HCHO) from space: validation and intercomparison of six retrievals from four satellites (OMI, GOME2A,
1195 GOME2B, OMPS) with SEAC4RS aircraft observations over the Southeast US, *Atmos. Chem. Phys.*, 0, 1-24,
1196 doi:10.5194/acp-2016-162, 2016.
- 1197 Zhou, Y., Brunner, D., Boersma, K. F., Dirksen, R., and Wang, P.: An improved tropospheric NO₂ retrieval
1198 for OMI observations in the vicinity of mountainous terrain, *Atmos. Meas. Tech.*, 2, 401-416, doi:10.5194/amt-
1199 2-401-2009, 2009.



1200 **APPENDIX A: Acronyms and abbreviations**

A	Averaging Kernel
AMF	Air mass factor
AOD	Aerosol optical depth
AAI	Aerosol absorbing index
ATBD	Algorithm Theoretical Basis Document
BIRA-IASB	Royal Belgian Institute for Space Aeronomy
BrO	Bromine Monoxide
BRDF	Bidirectional reflectance distribution function
CH ₄	Methane
CO	Carbon Monoxide
CAPACITY	Composition of the Atmosphere: Progress to Applications in the user CommuNITY
CCD	Charged Coupled Device
CF	Climate and Forecast metadata conventions
CRB	Clouds as Reflecting Boundaries
CTM	Chemical Transport Model
DOAS	Differential optical absorption spectroscopy
DU	Dobson Unit (1 DU = 2.6867x10 ¹⁶ molecules cm ⁻²)
ECMWF	European Centre for Medium Range Weather Forecast
ESA	European Space Agency
FWHM	Full Width Half Maximum
GMES	Global Monitoring for Environment and Security
GOME	Global Ozone Monitoring Experiment
HCHO	Formaldehyde (or H ₂ CO)
IPA	Independent Pixel Approximation
IR	Infrared
ISRF	Instrument Spectral Response Function
L2	Level-2
L2WG	Level-2 Working Group
LER	Lambertian Equivalent Reflector
VLIDORT	Vector LInearized Discrete Ordinate Radiative Transfer
LOS	Line-of-sight angle
LS	Lower stratosphere
LUT	Look-up table
MAX-DOAS	Multi-axis DOAS
MPC	Mission Performance Center
NDACC	Network for the Detection of Atmospheric Composition Change
NMVO	Non-Methane Volatile Organic Compound
NO ₂	Nitrogen Dioxide



NRT	Near-real time
OCRA	Optical Cloud Recognition Algorithm
OD	Optical Depth
O ₃	Ozone
OMI	Ozone Monitoring Instrument
OMPS	Ozone Mapping Profiler Suite
(P)BL	Planetary Boundary Layer
PCA	Principal Component Analysis
QA4ECV	Quality Assurance For Essential Climate Variables
RAA	Relative Azimuth Angle
ROCINN	Retrieval Of Cloud Information using Neural Networks
RRS	Rotational Raman Scattering
RTM	Radiative transfer model
S5P	Sentinel-5 Precursor
S5	Sentinel 5
SAA	Solar Azimuth Angle
SCIAMACHY	SCanning Imaging Absorption spectroMeter for Atmospheric ChartographY
SC(D)	Slant column density
SCDE	Slant column density error
SNR	Signal-to-noise ratio
SO ₂	Sulfur dioxide
SOW	Statement Of Work
SWIR	Short-wave infrared
SZA	Solar zenith angle
TM 4/5	Data assimilation / chemistry transport model (version 4 or 5)
TROPOMI	Tropospheric Monitoring Instrument
UPAS	Universal Processor for UV/VIS Atmospheric Spectrometers
UV	Ultraviolet
UVN	Ultraviolet/Visible/Near-infrared
VAA	Viewing Azimuth Angle
VZA	Viewing Zenith Angle
VC(D)	Vertical column density


 1201 **APPENDIX B: High level L2 HCHO data product description**

1202 In addition to the main product results, such as HCHO slant column, tropospheric vertical column and air mass
 1203 factor, the level 2 data files contain a number of additional ancillary parameters and diagnostic information. A
 1204 complete description of the level 2 data format is given in the Product User Manual (Pedergrana et al., 2017).
 1205 A selection of important parameters is given in Table 13. A complete description of the level 2 data format is
 1206 given in the Product User Manual (Pedergrana et al., 2017).

1207 **Table 13: Selective list of output fields in the TROPOMI HCHO product. Scanline and ground_pixel**
 1208 **are respectively the number of pixels in an orbit along track and across track. Layer is the number of**
 1209 **vertical levels in the averaging kernels and the a-priori profiles.**

Symbol	Unit*	Variable name	Number of entries
N_v	mol.m ⁻²	formaldehyde_tropospheric_vertical_column	scanline x ground_pixel
N_s	mol.m ⁻²	fitted_slant_columns	scanline x ground_pixel x number_of_slant_columns
$N_s - N_{s,0}$	mol.m ⁻²	formaldehyde_slant_column_corrected	scanline x ground_pixel
$N_{v,0}$	mol.m ⁻²	formaldehyde_tropospheric_vertical_column_correction	scanline x ground_pixel
M	n.u.	formaldehyde_tropospheric_air_mass_factor	scanline x ground_pixel
M_{clear}	n.u.	formaldehyde_clear_air_mass_factor	scanline x ground_pixel
f_c	n.u.	cloud_fraction_crb	scanline x ground_pixel
w_c	n.u.	cloud_fraction_intensity_weighted	scanline x ground_pixel
p_{cloud}	Pa	cloud_pressure_crb	scanline x ground_pixel
A_{cloud}	n.u.	cloud_albedo_crb	scanline x ground_pixel
A_s	n.u.	surface_albedo	scanline x ground_pixel
z_s	m	surface_altitude	scanline x ground_pixel
$\sigma_{N,v,rand}$	mol.m ⁻²	formaldehyde_tropospheric_vertical_column_precision	scanline x ground_pixel
$\sigma_{N,v,syst}$	mol.m ⁻²	formaldehyde_tropospheric_vertical_column_trueness	scanline x ground_pixel
$\sigma_{N,s,rand}$	mol.m ⁻²	fitted_slant_columns_precision	scanline x ground_pixel x number_of_slant_columns
$\sigma_{M,rand}$	n.u.	formaldehyde_tropospheric_air_mass_factor_precision	scanline x ground_pixel
$\sigma_{N,s,0}$	mol.m ⁻²	formaldehyde_slant_column_corrected_trueness	scanline x ground_pixel
A	n.u.	averaging_kernel	layer x scanline x ground_pixel
n_a	vmr	formaldehyde_profile_apriori	layer x scanline x ground_pixel
p_s	Pa	surface_pressure	scanline x ground_pixel
a_l	Pa	tm5_constant_a	layer



Symbol	Unit*	Variable name	Number of entries
b_l	n.u.	tm5_constant_b	layer
$N_{s,l}$	mol.m ⁻²	fitted_slant_columns_win1	scanline x ground_pixel x number_of_slant_columns_win1
$\sigma_{N,s,1,rand}$	mol.m ⁻²	fitted_slant_columns_precision_win1	scanline x ground_pixel x number_of_slant_columns_win1

1210 * multiplication factor to convert mol.m⁻² to molec.cm⁻²: 6.022x10¹⁹


 1211 **APPENDIX C: Averaging Kernel**

1212 Retrieved satellite quantities always represent a weighted average over all parts of the atmosphere that
 1213 contribute to the signal observed by the satellite instrument. The DOAS total column retrieval is implicitly
 1214 dependant on the a priori trace gas profile n_a . Radiative transfer calculations account for the sensitivity of the
 1215 measurement to the HCHO concentrations at all altitudes and these sensitivities are weighted with the assumed
 1216 a priori profile shape to produce the vertical column. The averaging kernel (A) is proportional to the
 1217 measurement sensitivity profile, and provides the relation between the retrieved column N_v and the true tracer
 1218 profile x (Rodgers, 2000; Rodgers and Connor, 2002):

$$N_v - N_{v,a} = A \cdot (x^{pc} - n_a^{pc}) \quad (21)$$

1219 where the profiles are expressed in partial columns (pc). For total column observations of optically thin
 1220 absorbers DOAS averaging kernels are calculated as follows (Eskes and Boersma, 2003): $A(p) = \frac{m(p)}{M}$, where
 1221 $m(p)$ is the altitude-resolved air mass factor and M is the tropospheric air mass factor. The air mass factor and
 1222 therefore the retrieved vertical column, depends on the a priori profile shape, in contrast to the altitude-resolved
 1223 air mass factor which describes the sensitivity of the slant column to changes in trace gas concentrations at a
 1224 given altitude and does not depend on the a priori profile in an optically thin atmosphere. From the definition
 1225 of A , we have $N_{v,a} = A \cdot n_a^{pc}$ and Equation (21) simplifies to:

$$N_v = A \cdot x^{pc} \quad (22)$$

1226 The averaging kernel varies with the observation conditions. In the HCHO retrieval product, A is provided
 1227 together with the error budget for each individual pixel. The provided HCHO vertical columns can be used in
 1228 two ways, each with its own associated error (Boersma et al., 2004):

- 1229 1. For independent study and/or comparison with other independent measurements of total column amounts.
 1230 In this case, the total error related to the column consists of slant column measurement errors, reference
 1231 sector correction errors, and air mass factor errors. The latter consists of errors related to uncertainties in
 1232 the assumed profile n_a and errors related to the m parameters.
- 1233 2. For comparisons with chemistry transport models or validation with independent profile measurements,
 1234 if the averaging kernel information is used, the a priori profile shape error no longer contributes to the
 1235 total error. Indeed, the relative difference between the retrieved column N_v and an independent profile x_i
 1236 is:

$$\delta = \frac{N_v - A \cdot x_i^{pc}}{N_v} \quad (23)$$

1237



1238 The total AMF M cancels since it appears as the denominator of both N_p and A . Because only the total
1239 AMF depends on the a priori tracer profile n_a , the comparison using the averaging kernel is not influenced
1240 by the chosen a priori profile shape. The a priori profile error does not influence the comparison, but of
1241 course, it still does influence the error on the retrieved vertical column.